




## Topological multimode waveguide QED

C. Vega , D. Porrás , and A. González-Tudela 

*Institute of Fundamental Physics IFF-CSIC, Calle Serrano 113b, 28006 Madrid, Spain*



(Received 8 July 2022; accepted 28 March 2023; published 17 April 2023)

Topological insulators feature a number of topologically protected boundary modes linked to the value of their bulk invariant. While in one-dimensional systems the boundary modes are zero dimensional and localized, in two-dimensional topological insulators the boundary modes are chiral, one-dimensional propagating modes along the edges of the system. Thus, topological photonic insulators with large Chern numbers naturally display a topologically protected multimode waveguide at their edges. Here, we show how to take advantage of these topologically protected propagating modes by interfacing them with quantum emitters. In particular, using a Harper-Hofstadter lattice, we find situations in which the emitters feature quasiquantized decay rates due to the increasing number of edge modes, and where their spontaneous emission spatially separates in different modes. We also show how using a single  $\pi$  pulse the combination of such spatial separation and the interacting character of the emitters leads to the formation of a single-photon time-bin entangled state with no classical analog, which we characterize computing its entanglement entropy. Finally, we also show how the emitters can selectively interact with the different channels using nonlocal light-matter couplings such as the ones that can be obtained with giant atoms. Such capabilities pave the way for generating quantum gates among topologically protected photons as well as generating more complex entangled states of light in topological channels.

DOI: [10.1103/PhysRevResearch.5.023031](https://doi.org/10.1103/PhysRevResearch.5.023031)

### I. INTRODUCTION

Topological photonics [1–4] is a burgeoning field aiming at exporting topological concepts into photonics to bring novel, and more robust, ways of controlling the properties of light. At the classical level, one of the original motivations of the field was to exploit the chiral, edge modes appearing in two-dimensional topological insulators to obtain unidirectional and robust-to-disorder photon flows [5,6]. In their simplest instance, that is, when only a single edge mode appears, it was soon realized in several platforms [7–9]. Remarkably, these realizations opened up applications beyond their initial motivation, such as the design of “topological lasers” [10–13] and chiral light-matter couplings [14–18], or the generation of Gaussian quantum correlations with parametric drivings [19–25]. Besides, they have been proposed as robust *quantum buses* for quantum state transfer [26–29], without the exponential time dependence on their distance of their zero-dimensional counterparts [30–36]. The more complex scenario when the two-dimensional system features several edge modes [37,38] opens up new opportunities, e.g., to increase quantum communication capacity using several topologically protected channels. Remarkably, this situation has been much more scarcely explored in the literature, likely because it is still unclear how to profit from these extra modes. Coupling quantum emitters to such structures

provide a natural route to harness these additional degrees of freedom. On the one hand, local light-matter coupling enables the coupling to all photonic modes at the emitter frequencies, thus it is able to interact with several modes simultaneously. This has already been shown to lead to unconventional emitter-emitter interactions when coupled to the bulk modes of one-dimensional [39–41], two-dimensional [40,42], and three-dimensional [43,44] topological insulators. Besides, the strongly interacting character of the emitters can induce (non-Gaussian) quantum correlations beyond the ones that can be obtained with parametric drivings [19–25], opening a path to observe exotic quantum many-body states [45–50]. All these reasons are motivating the development of such topological light-matter interfaces in various platforms, ranging from superconducting qubits coupled to microwave resonators [18,51] to solid-state emitters coupled to topological photonic crystals [14–17]. In this work, we develop a theory for the topological multimode waveguide QED scenario that appears when quantum emitters couple to the edges of topological photonic insulators with large Chern numbers. The physics emerging from this scenario is very different from the case of emitters coupled to one-dimensional topological insulators [39–41], where the localized nature of the boundary modes leads generally to coherent emitter dynamics/interactions rather than irreversible or collective decay dynamics. Using that theory, in Sect. II we unveil the entanglement structure of the spontaneously emitted photons in such topological multimode waveguides, and show that one can obtain almost maximally entangled  $W$ -type states between the edge channels. Besides, combining several  $\pi$  pulses [52], we show that one can obtain strongly correlated multiphoton states. Finally, in Sec. IV we also devise a method that enables

*Published by the American Physical Society under the terms of the Creative Commons Attribution 4.0 International license. Further distribution of this work must maintain attribution to the author(s) and the published article's title, journal citation, and DOI.*

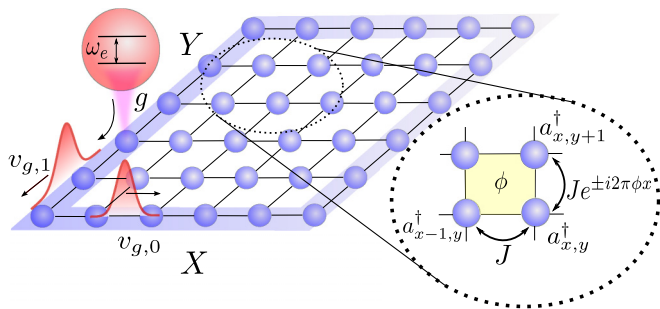


FIG. 1. Topological light-matter interface: Blue globes represent lattice sites, with annihilation (creation) operators  $a_{x,y}^{(\dagger)}$ . The yellow-shaded region denotes a single lattice plaquette with flux  $\phi$ . We also represent the spontaneous emission of an emitter (in red) coupled to the the lattice edge, which radiates through all edge modes (two in the figure), that propagate at different group velocities (denoted by  $v_{g,0}$  and  $v_{g,1}$ ), causing a spatial separation of the emitted pulse.

the emitters to interact selectively with the different topological channels using giant atoms [53–58].

## II. MODEL

The model that we consider in this paper is depicted in Fig. 1(a): A quantum emitter interacts locally with one of the edges of a two-dimensional topological insulator. Motivated by recent experiments [18], we particularize for a square photonic lattice with nearest-neighbor hoppings of rate  $J$ , subject to an effective magnetic flux  $\phi$ —the so-called Harper-Hofstadter (HH) lattice [59]—where bands with large Chern number appear for small magnetic fluxes [60,61]. The bath Hamiltonian then reads (setting  $\hbar = 1$ )

$$H_B = -J \left( \sum_{x,y} a_{x+1,y}^\dagger a_{x,y} + e^{-2\pi i \phi x} a_{x,y+1}^\dagger a_{x,y} \right) + \text{H.c.}, \quad (1)$$

where  $a_{x,y}^{(\dagger)}$  represent the annihilation (creation) operator at the  $(x, y)$  position, and where we take the cavity energy as the energy reference. The emitter is assumed to have a single optical transition between its ground ( $g$ ) and excited ( $e$ ) states with frequency  $\omega_e$ , that couples to one of the photonic lattice sites at the edges through the standard light-matter Hamiltonian,  $H_I = (g a_{x_e, y_e} \sigma_{eg} + \text{H.c.})$ , with  $g$  being its coupling strength,  $(x_e, y_e)$  the position where it couples, and  $\sigma_{\alpha\beta} = |\alpha\rangle\langle\beta|$  the emitter’s operators. The emitter’s Hamiltonian then reads  $H_S = \omega_e \sigma_{ee}$ , such that the full topological light-matter Hamiltonian reads  $H = H_S + H_B + H_I$ . The HH model displays a very rich behavior depending on the value of  $\phi$  [59–61]. here, we take  $\phi = 1/q$ , with  $q \in \mathbb{N}$ , that is enough to illustrate the behavior we are interested in. With this parametrization, the spectrum of the system with periodic boundary conditions features  $q$  bands, labeled as Landau levels [60], separated by  $l = 0, \dots, q-1$  band gaps. Besides, it can be shown that the first  $\lfloor (q-1)/2 \rfloor$  bands (with  $\lfloor \cdot \rfloor$  being the floor function) have an associated quantized Chern number  $C = -1$  [60]. Thus, with open boundary conditions, it is expected that the  $l$ th band gap features  $2(l+1)$  gapless edge states, associated with the  $l+1$  Landau levels below that energy [62]. To illustrate this, we consider a cylinder geometry

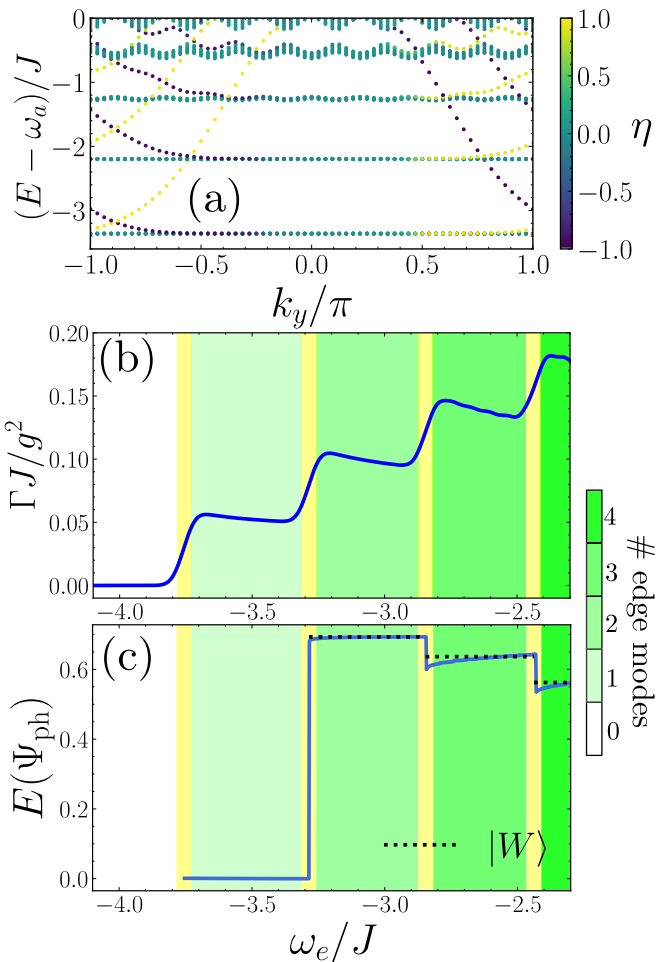


FIG. 2. (a) HH spectrum with periodic boundary conditions in the  $Y$  direction and open boundary conditions in the  $X$  direction, for  $\phi = 1/9$  and a lattice size of  $65 \times 65$  sites. Each dot is colored according to the localization parameter  $\eta$  defined in the main text:  $\eta = 0$  corresponds to a delocalized state, while  $\eta = (-)1$  depicts complete localization at the (left) right boundary. (b) Emitter spontaneous emission rate as a function of its transition frequency  $\omega_e$  approximating  $\delta(\omega_e - E)$  by a Gaussian function with mean  $\omega_e - E_B$  and width  $\theta = 0.07J$ . The emitter is coupled to the edge of a HH lattice of size  $150 \times 150$  with flux  $\phi = 1/25$ . Yellow vertical fringes are centered at Landau levels and have a width equal to  $\theta$ . (c) Entanglement entropy,  $E(\Psi_{\text{ph}})$ , of the emitted single-photon state in the asymptotic limit, as a function of the emitter energy, for the same lattice parameters as panel (b).

for the bath with periodic (open) boundary conditions in the  $Y$  ( $X$ ) direction. This allows one to write the spatial wave function of the bath eigenstates as  $\psi_l(x, y) = e^{ik_y y} \Psi_l(x)$ , and calculate their eigenenergies  $\omega(k_y)$  numerically. In Fig. 2(a), we plot an example of the bath spectrum for a bath with  $\phi = 1/9$  and  $65 \times 65$  sites, showing the emergence of the gapless modes between the bulk flat bands. Besides, we define a localization parameter  $\eta = \sum_{x=0}^{L-1} (-1 + 2 \frac{x}{L-1}) |\Psi(x)|^2$ , that ranges  $\eta \in [-1, 1]$ , achieving the extremes  $(-1)$  when the modes are maximally localized at the left (right) edge, encoded in purple (yellow) color, respectively, in Fig. 2(a). In this way one can see how, for energies below  $\omega_a$ , the edge modes at the left

(right) have always negative (positive) group velocity along  $Y$ , and thus have a chiral character. Thus, when coupling an emitter to one of the edges, it will only interact with the modes of certain chirality. An important observation from Fig. 2(a) is that the edge-mode dispersions deviate significantly from the linear behavior typically assumed in the literature for such topological channels [26–28]. Since this can have important consequences in the quantum optical behavior, we derive a more accurate effective description of these modes for  $\phi \ll 1$ , showing that the edge-mode dispersion for the left-localized states emerging from the  $l$ th Landau level is approximated by

$$\omega_l(k_y) \approx \omega_{LL}(\phi) + a_l(\phi)[k_y - k_l(\phi)]^2, \quad (2)$$

for  $(k_y - k_l(\phi)) \in (-\pi, 0)$ . Here,  $\omega_{LL}(\phi)/J \approx -4 + 4\pi\phi(l + \frac{1}{2}) - (\pi\phi)^2(l^2 + l + 1/2)$  is the energy of the  $l$ th Landau level [60],  $a_l(\phi)$  is the effective curvature of the edge modes which we extract from numerical fittings, and which converges to  $a_l(\phi \rightarrow 0) \sim 0.6$ , and  $k_l(\phi)$  is the momentum resonant to the minimum edge-mode energy. Besides, the spatial distribution of these modes along the  $X$  direction is  $\Psi_l(x) = \sqrt{2/\lambda_l(\phi)}e^{-x/\lambda_l(\phi)}$ , where  $\lambda_l$  grows as  $\phi \rightarrow 0$  as expected, since in  $\phi = 0$  we should recover the delocalized bath eigenstates of the standard square lattice model.

### III. SPONTANEOUS EMISSION FEATURES IN MULTIMODE WAVEGUIDE QED

Let us now see how coupling emitters to the edge of the HH lattice leads to several unique phenomena. First, let us note that since the emitter probes the system at fixed frequency,  $\omega_e$ , one can control the number of modes that will be relevant for its dynamics just by adjusting its relative detuning with the bath energies. A magnitude that evidences that control is the Markovian decay rate defined by [63]

$$\Gamma(\omega_e) = \sum_{E_B} |\langle e|H_I|E_B\rangle|^2 \delta(\omega_e - E_B), \quad (3)$$

with  $|E_B\rangle$  being the bath eigenstates, i.e.,  $H_B|E_B\rangle = E_B|E_B\rangle$ , for the considered configuration. In Fig. 2(b), we plot with a blue solid line the expected  $\Gamma(\omega_e)$  for an emitter coupled to the edge of a HH lattice for  $\phi = 1/25$  as a function of  $\omega_e$ . There, we see how the expected decay rate abruptly increases from one band-gap to the other as the emitter's energy is varied. The jumps occur when the emitter's energy  $\omega_e$  starts crossing the Landau level energies, indicated by the shaded yellow region in the figure, due to the emergence of another edge mode that couples to the emitter. Note also that the decay rate remains almost constant along the whole band-gap region, except for a deviation that occurs due to the nonlinear energy dispersion of the modes. As shown in the Appendix B, this quasiquantized behavior is well captured by our effective model, which gives a semianalytical approximation for the decay rates into the different topological channels  $\Gamma_l(\omega_e)$ , that reproduces the nonlinear dependence with the frequency, i.e.,

$$\Gamma_l(\omega_e) \sim (\omega_e - \omega_{LL})^{-1/2}. \quad (4)$$

As expected, the total decay is then obtained by summing the contributions of the active channels, i.e.,  $\Gamma = \sum_l \Gamma_l$ . A

more remarkable feature of these topological multi-mode waveguide scenarios is what occurs with the spontaneously emitted photons when the emitters are driven. Let us first assume a perfect  $\pi$ -pulse driving which prepares the system in the state  $|\Psi_0\rangle = |e\rangle \otimes |\text{vac}\rangle$ , with  $|\text{vac}\rangle$  being the bath state with no photons. When the laser is switched off, the whole system evolves according to the total Hamiltonian  $|\Psi(t)\rangle = e^{-iHt}|\Psi_0\rangle$ , leading eventually to a single-photon wave-packet state

$$|\Psi(t \rightarrow \infty)\rangle = |g\rangle \otimes \sum_{x,y} A(x,y) a_{x,y}^\dagger |\text{vac}\rangle, \quad (5)$$

as occurs in other quantum optical setups [64]. However, in this case such wave packets have unique features which we illustrate in Fig. 3 for an emitter coupled to the edge of a HH lattice with  $\phi = 1/9$ . First, irrespective of the band gap that the emitters are resonant to, the photons are emitted in a chiral and robust fashion due to their topological origin. This is illustrated in Figs. 3(a), 3(c), and 3(e), where we plot the full photonic bath population,  $|A(x,y;t)|^2$ , at a time  $TJ = 200$ . There, we observe that the single-photon wave packet can overcome the defect introduced in one of the edges without altering significantly its propagation. Besides, we also observe how the situations with more than one edge state, Figs. 3(c) and 3(e), display a localized, but more complex, wave function. To appreciate better the inner structure of these wave packets, we plot in Figs. 3(b), 3(d), and 3(f) their temporal dynamics, focusing only on the edge population,  $|A(0,Y;t)|^2$ . In this way we observe a unique effect of these multimode wave guides; that is, after certain time, the emission into the different topological channels becomes spatially separated due to the different group velocities of the modes at the emitter frequency. Intuitively, this separation starts to occur for times such that  $|v_{g,l} - v_{g,l'}|T \gtrsim \Gamma_l^{-1} + \Gamma_{l'}^{-1}$ ; that is, that the separation between the wave packets is larger than their intrinsic linewidth ( $\Gamma_l^{-1}$ ). When this separation occurs, one can say that our emitter has generated single-photon entangled states [65] between orthogonal time bins  $T_l$ . Defining  $|1\rangle_l$  as the presence of a photon in the  $T_l$  time bin and 0 in the rest, the photonic state created in the asymptotic limit can be written as

$$|\Psi(t \rightarrow \infty)\rangle_{\text{ph}} \approx \sum_l c_l |1\rangle_l. \quad (6)$$

Using that, one can calculate the entanglement entropy [66],  $E(\Psi_{\text{ph}})$ , of the asymptotic state in the different band gaps, the result of which is shown in Fig. 2(c) and compared with the one of a perfect  $W$ -entangled state [67] as a black dashed line. There, we observe how the entanglement entropy of the emitted state indeed approximates that of a maximally entangled state. Note that in more conventional quantum optical setups [52,68–83] where such time-bin entanglement is generated it is required to combine superpositions in multilevel emitters and multiple drivings, while here already with a single  $\pi$  pulse a  $W$ -type [67] entangled structure appears due to the multimode nature of the waveguide. Applying several  $\pi$  pulses, one can obtain more complex multiphoton states. For example, if a second  $\pi$  pulse is applied at a time  $T_D$  before the excitation from the first  $\pi$  pulse decays completely, the emission of the second photon is correlated with the first. As shown in Ref. [52], this ends up generating two-photon Bell-like states

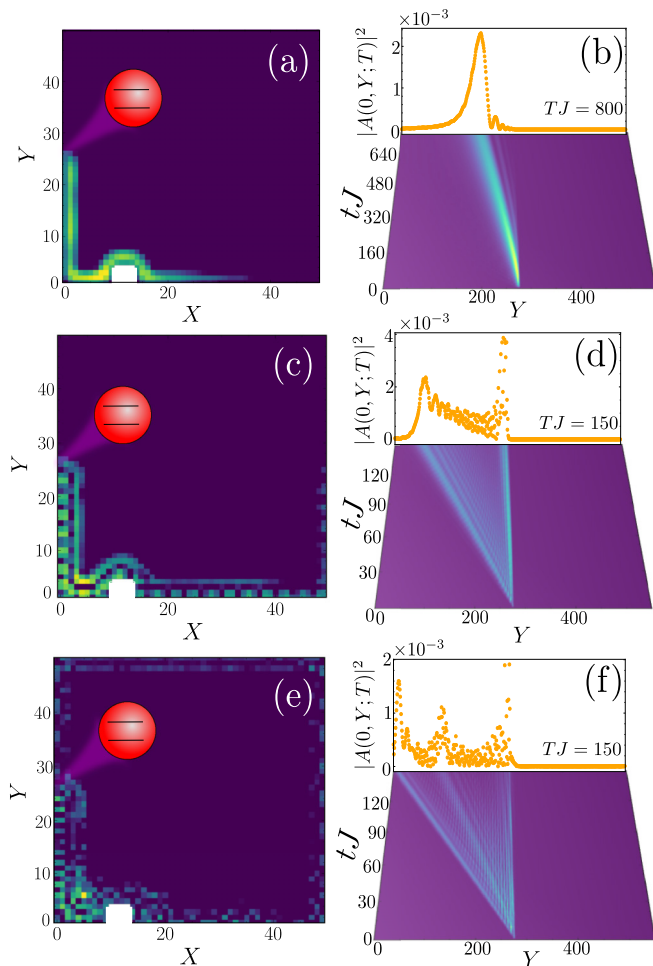


FIG. 3. Spontaneous emission features of a quantum emitter coupled to the middle site of the left boundary of a HH lattice for  $\phi = 1/9$ , with quantum emitter frequencies of  $\omega_e/J = -3.31$  (first row),  $\omega_e/J = -2.16$  (second row), and  $\omega_e/J = -1.25$  (last row), resonant to one, two, and three edge modes respectively. (a), (c), (e) Snapshots at  $TJ = 200$  of the bath population in real space for a lattice size of  $50 \times 50$  and a coupling constant of  $g/J = 0.1$ , in the presence of a defect, depicted as a white-colored region in the lowest part of the lattice. (b), (d), (f) Dynamics of the emitted photon. For each  $\omega_e$ , we plot the evolution of the population of the left boundary sites  $|A(0, Y; t)|^2$ , in arbitrary units. At the top, we include a snapshot of the pulse shape at the final time instant, showing one, two, and three peaks respectively, which correspond to the number of resonant edge modes in each case.

in the photon number basis

$$|\Psi_{\text{Bell}}\rangle \propto (1 + a_{E(L)}^\dagger a_L^\dagger)|\text{vac}\rangle, \quad (7)$$

where  $a_{E(L)}^\dagger$  represents the photon operator emitted from the first (second)  $\pi$  pulse. Compared to Ref. [52], in the topological multimode setups the single-photon wave packets already have an internal superposition structure,  $a_{E(L)}^\dagger \propto \sum_l c_{E(L),l} a_l^\dagger |\text{vac}\rangle$ , with  $a_l^\dagger$  being the effective operator associated with the photon emitted in the  $l$ th topological channels. Therefore, its multiphoton structure will be much richer, and depends on the interplay between the pulse delay  $T_D$ , the global  $\Gamma$  and individual  $\Gamma_l$  decay times, and the asymptotic

time where it is measured. Let us emphasize that the non-Gaussian character of these states is a consequence of the strongly interacting character of the emitters, and could never be obtained in classical setups.

#### IV. MODE SELECTIVITY VIA NONLOCAL COUPLINGS

Finally, let us show how to make the emitters interact selectively with one of the resonant channels. The key idea is to couple the emitter with more than a single lattice site, as can be done with giant atoms [53–57]. Let us illustrate it in the simplest case where we want to cancel only one resonant momentum. This requires that the emitter couples to two adjacent cavities with the same strength, and relative phase  $e^{i\varphi}$ , i.e.,  $g_{(0,y)} = g$  and  $g_{(0,y+1)} = ge^{i\varphi}$ . In that case, the  $\mathbf{k}$ -dependent light-matter coupling reads

$$|G_\varphi(k_y)|^2 \propto [1 + \cos(k_y + \varphi)], \quad (8)$$

and thus it vanishes at  $k_y = k_e$  if we choose  $\varphi = \pi - k_e$ . This was the key idea introduced in single-mode waveguide QED setups [84–86] to obtain chiral emission. Here, the emission is already chiral, but we can still use it to cancel the emission into the resonant momenta of the undesired resonant channels. In Fig. 4 we show a proof-of-principle realization of that idea for a situation when the emitter is resonant to two edge modes. In Fig. 4(a), we plot the energy spectrum for a lattice with  $\phi = 1/12$  and  $65 \times 65$  sites. The solid horizontal red line indicates the energy of the emitter that is chosen in the second band gap to be resonant to two channels with resonant momenta  $k_e^{(0)}$  and  $k_e^{(1)}$ , indicated by vertical dotted black lines. This means that if the emitter couples locally, it will couple to the two  $k$  channels, as shown in Fig. 4(b), and emit in a two-mode fashion in real space, as shown by black dots in Fig. 4(e). In contrast, if we choose nonlocal couplings to cancel the coupling to either the momentum  $k_e^{(0)}$  or  $k_e^{(1)}$ , as depicted by orange and blue dotted lines in Fig. 4(a), one can see that the emitter selectively emits only in one of the channels, as illustrated in Figs. 4(c)–4(e) by plotting snapshots of the population in momentum space and real space. In particular, in Fig. 4(e) where we plot a snapshot at time  $TJ = 150$  of the spatial profile of the emitted pulse for the different coupling choices, we observe very clearly that the designed nonlocal couplings suppress the emission onto the selected mode compared to local light-matter coupling situation. In the Appendix C we also prove that the number of nonlocal couplings required to cancel  $N_k$  resonant momenta scales only linearly with  $N_k$ . This mode selectivity is an interesting tool in this scenario because when a photon propagates in a chiral channel and interacts with an emitter it acquires a  $\pi$  phase [87]. Thus, if multiple photons are sent in the different channels, such mode selectivity can lead to different phases between the topologically protected photons. This can be a resource for generating photon gates among topologically protected photons by adapting existing protocols [88].

#### V. CONCLUSIONS AND OUTLOOK

Summing up, we characterize the topological multimode waveguide QED setup that appears when quantum emitters



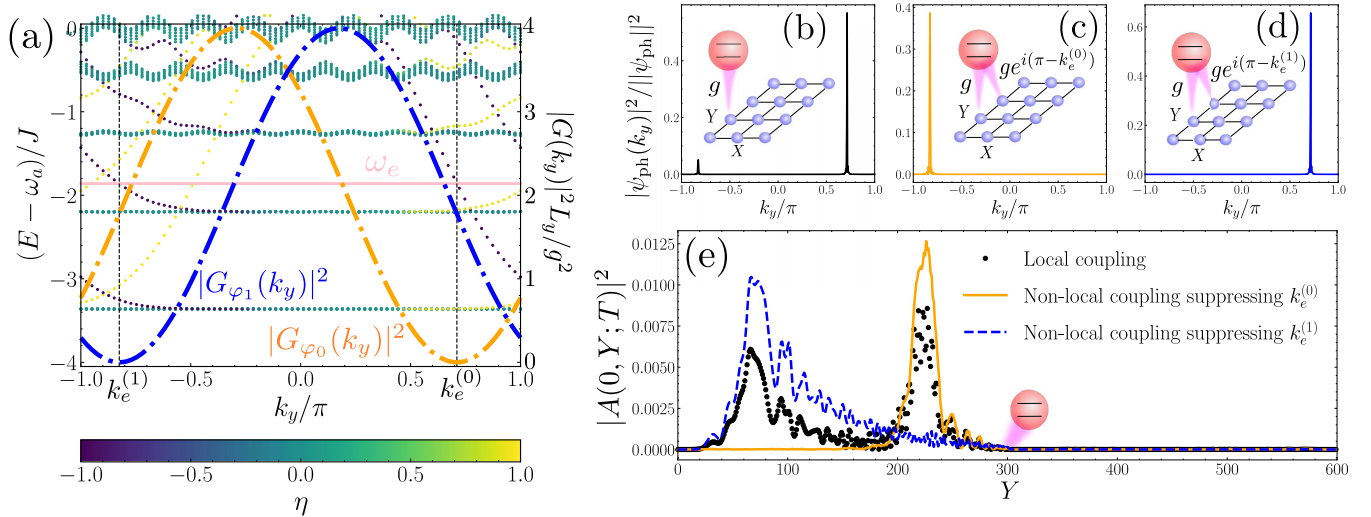


FIG. 4. (a) Spectrum of a HH lattice of  $65 \times 65$  sites for  $\phi = 1/12$ . Each dot is colored according to the localization index  $\eta$  as in Fig. 2(a). The solid pink line depicts the quantum emitter frequency  $\omega_e/J = -1.86$ , that is resonant to two left-localized edge modes at momenta  $k_e^{(0)}$  and  $k_e^{(1)}$  respectively. We prove mode selectivity using nonlocal couplings that in momentum space are of the form  $|G_{\varphi_0}(k_y)|^2$  and  $|G_{\varphi_1}(k_y)|^2$ , represented as dash-dotted lines, whose units are indicated in the right vertical axis, and are analytically described in Eq. (8). Note that the orange (blue) line, representing  $|G_{\varphi_0}(k_y)|^2$  ( $|G_{\varphi_1}(k_y)|^2$ ) vanishes at  $k_e^{(0)}$  ( $k_e^{(1)}$ ). (b), (c), (d) Normalized photon population in momentum space for the photonic state resulting from spontaneous emission at time  $TJ = 300$  of a quantum emitter with energy  $\omega_e/J = -1.86$  coupled to the left edge of a HH lattice of size  $250 \times 250$  and  $\phi = 1/12$ . The emitter coupling is (b) local and [(c), (d)] nonlocal, designed to cancel emission at  $k_e^{(0)}$  and  $k_e^{(1)}$  respectively. (e) Snapshot at time  $TJ = 150$  of the photonic state in the left lattice boundary, coming from spontaneous emission in the three distinct coupling configurations, with same values for  $\omega_e$  and  $\phi$ . The lattice size is  $600 \times 600$ , and the light-matter coupling constant is  $g/J = 0.2$ .

couple to the edges of a Harper-Hofstadter lattice. We find several unique features such as the quasiquantization of the decay rates and the *spontaneous* generation of entanglement in the different topological channels, as well as a way to make the emitters interact selectively with some of the channels. We foresee that the combination of these setups with multilevel emitters and/or complex time-dependent [52,68–83] or parametric [19–25] drivings can be used to generate more complex states of light in these topologically protected channels either in a transient [19,20,22,24,25,89–91] or a steady-state fashion [92–101], as well as to induce gates between topologically protected photons [88]. Although we find our results for the Harper-Hofstadter model, we expect our findings can be of interest to other systems where such multiple edge states appear [37,38,102–104]. Recently, another work studying the coupling of emitters to the edges of two-dimensional photonic insulators appeared [105], although it focused only on the single-edge-mode scenario.

#### ACKNOWLEDGMENTS

The authors acknowledge useful discussions with Geza Giedke and Alberto Muñoz de las Heras. The authors acknowledge support from the Proyecto Sinérgico CAM 2020 Y2020/TCS-6545 (NanoQuCo-CM), from the CSIC Research Platform on Quantum Technologies PTI-001, and from Spanish project PID2021-127968NB-I00 (MCIU/AEI/FEDER, EU). A.G.-T. also acknowledges support from a 2022 Leonardo Grant for Researchers and Cultural Creators, BBVA Foundation.

#### APPENDIXES

In these appendixes, we provide the details of the calculations supporting this paper. In Appendix A, we describe the main characteristic of the spectrum of the topological photonic lattice we consider, explaining how we calculate the spectrum for open and periodic boundary conditions. In Appendix B, we focus on the edge modes, and show how their features can be captured by a simple phenomenological model. In Appendix C, we give more details of the distinctive features of the spontaneous emission of emitters coupled to the edge of these systems, such as their expected decay rates and the spontaneous spatial separation of the photonic emission patterns.

#### APPENDIX A: CHARACTERIZATION OF THE HARPER-HOFSTADTER LATTICE MODEL

The Harper-Hofstadter (HH) model that we consider in this paper is a two-dimensional bosonic lattice where time-reversal symmetry is broken by an artificial gauge field introduced through a Peierls phase [59–61]. Denoting by  $a_{\mathbf{r}}^{(\dagger)}$  the annihilation (creation) operators of the bosonic mode at site  $\mathbf{r} = (x, y)$  of the lattice, the HH Hamiltonian can be written (setting  $\hbar = 1$  herein)

$$H_B = -J \left( \sum_{x,y} (a_{x+1,y}^\dagger a_{x,y} + e^{-2\pi i \phi x} a_{x,y+1}^\dagger a_{x,y}) + \text{H.c.} \right), \quad (\text{A1})$$

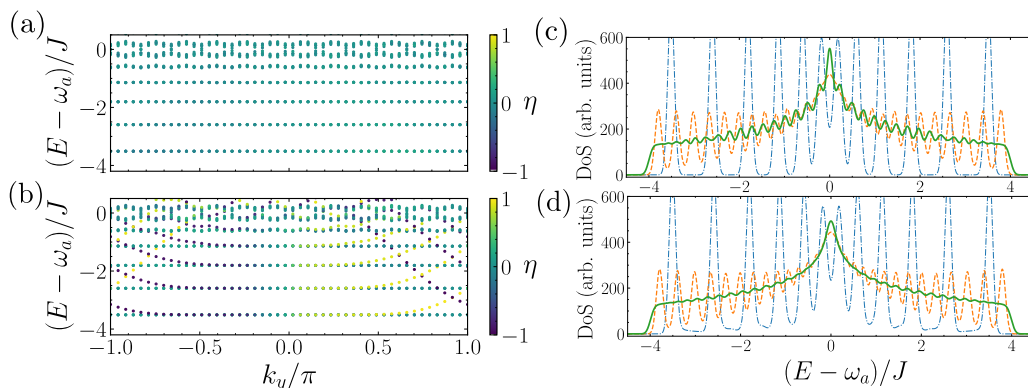


FIG. 5. (a), (b) Spectrum of a HH lattice of with (a) toroidal and (b) cylinder topology, for a magnetic flux  $\phi = 1/12$  and a system size of  $48 \times 48$  sites. When periodic boundary conditions are imposed over both spatial directions, panel (a), the lower part of the spectrum consists of a series of flat bands. If a boundary is opened, edge-localized, gapless excitations emerge at band-gap energies, panel (b). The color of each dot is assigned according to the localization parameter  $\eta$  defined in Eq. (A8) (c), (d) Density of states (DoS) of a HH lattice as defined in Eq. (A3) for the same lattice size, for different values of  $\phi$ :  $1/12$  (dash-dotted blue line),  $1/30$  (dashed orange line), and  $0$  (solid green line). The topology of the lattice is (c) toroidal and (d) cylindrical. For  $\phi \neq 0$ , the DoS exhibits divergences at Landau levels. As  $\phi \rightarrow 0$ , a Van Hove divergence is formed at the middle of the spectrum, which is a typical feature of a standard tight-binding square lattice with nearest-neighbor hoppings. The most relevant difference between both instances is that, for cylinder topology, the DoS deviates from zero in the band gaps due to the presence of topological edge modes. For these fluxes and system size, the ratios between the magnetic lengths  $l_B$  and the system size  $L = 48$  are  $l_B/L \approx 0.03$ ,  $l_B/L \approx 0.05$ , and  $l_B/L = \infty$  respectively. Both DoS have been obtained using an auxiliary width [as expressed in Eq. (A5)] of  $\theta/J = 0.1$ .

where we have assumed that time-reversal symmetry is broken by an artificial uniform magnetic field in the direction perpendicular to the direction of the lattice, whose strength is encoded in the value of complex phase  $\phi$  acquired in the nearest-neighbour hopping  $J$  along the  $Y$  direction. Note that we have also dismissed local cavity energy terms  $\omega_a \sum_{\mathbf{r}} a_{\mathbf{r}}^\dagger a_{\mathbf{r}}$ , assuming all cavity energies to be the same along the lattice  $\omega_{\mathbf{r}} = \omega_a$ , and therefore considering it as the energy reference of the problem, setting  $\omega_a \equiv 0$ . Then, there are three magnitudes that determine the shape of the spectrum and eigenmodes of the system:  $J$ ,  $\phi$ , and the system size  $L_x \times L_y$ . Let us start analyzing the spectrum of the system by imposing periodic boundary conditions along the  $X$  and  $Y$  directions, so that momentum  $\mathbf{k} = (k_x, k_y)$  is a good quantum number running over the values  $k_\alpha = -\pi, -\pi + 2\pi/L_\alpha, \dots, \pi - 2\pi/L_\alpha$ . As we said in the main text, we will restrict the analysis to rational values of  $\phi = p/q$ , with  $(p, q)$  being coprimes. This simplifies the diagonalization of the Hamiltonian, since one can write an effective unit cell that describes the bath lattice of  $1 \times q$  sites. With that unit cell, and using a plane-wave expansion to account for the periodicity of the lattice, we find that the bath Hamiltonian is given by  $q$  bands due to the degeneracy introduced by the supercell:

$$H_B = \sum_{\alpha=1}^q \sum_{\mathbf{k}} \omega_\alpha(\mathbf{k}) c_{\alpha,\mathbf{k}}^\dagger c_{\alpha,\mathbf{k}}, \quad (\text{A2})$$

where  $\alpha$  is the index running over the different bands, and  $c_{\alpha,\mathbf{k}}^{(\dagger)}$  are the operators describing the eigenstates of the bath for a given band  $\alpha$  and momentum  $\mathbf{k}$ . In Fig. 5(a), we plot an example of that bulk spectrum for  $\phi = 1/12$  and system size  $L_x = L_y = 48$ . There, we see the emergence of  $q$  almost flat bands well separated in energies. These are the so-called Landau levels that appear in such a model [59–61], and which describe a cyclic motion of lattice excitations whose radius

in lattice constant units is given by the *magnetic length*,  $l_B = 1/\sqrt{2\pi\phi}$ . Thus, in order for this Landau level picture to survive, it is required that this orbit fits in the lattice, i.e.,  $l_B \ll L_\alpha$ . When this condition is not satisfied, the spectrum tends to the square-lattice tight-binding spectrum  $\omega(k) = \omega_a - 2J[\cos(k_x) + \cos(k_y)]$ . This transition can be observed in the bath density of states (DoS), defined as

$$\text{DoS}(E) = \sum_{E_B} \delta(E - E_B), \quad (\text{A3})$$

where the sum is performed over all the bath eigenenergies  $E_B$ . Since the Dirac  $\delta$  has only mathematical sense in the continuum limit, for the finite systems we consider we approximate it by a Gaussian distribution of width  $\theta$ , that is

$$\text{DoS}(E) \approx \sum_{E_B} f_\theta(E - E_B) \quad (\text{A4})$$

with  $f_\theta(E - E_B)$ :

$$f_\theta(E - E_B) = \frac{1}{\sqrt{2\pi\theta^2}} \exp\left(-\frac{(E - E_B)^2}{2\theta^2}\right). \quad (\text{A5})$$

Using that trick, we plot the DoS of the Harper-Hofstadter Hamiltonian in Fig. 5(c), as a function of  $\phi$  for a fixed system size, showing the transition from the  $q$ -separated band to a unique band with a Van Hove singularity at the central energy  $\omega_a$ , characteristic of the nearest-neighbor two-dimensional tight-binding model. An important characteristic of these energy bands that appear in the bulk spectrum is that they can have a nonzero quantized topological invariant associated with them, that is, the Chern number. In fact, it can be shown that the Chern number of the  $l$ th band is given by  $C_l = t_l - t_{l-1}$ , where the  $t_l$  are integer numbers obtained by

solving the Azbel-Hofstadter Diophantine equation [60,61]:

$$l + 1 = qs_l + pt_l \quad \text{with } |t_l| < \frac{q}{2}, \quad (\text{A6})$$

where  $t_{-1} = 0$ . Notice that the relation  $C_l = t_l - t_{l-1}$  implies that  $t_l = \sum_{l' < l} C_{l'}$ , i.e., the topological index  $t_l$  reveals the sum of the Chern numbers of the lowest  $l$  bands. For example, in the case of  $\phi = 1/q$  considered in the main text, it results that the first  $[(q-1)/2]$  bands (letting  $[\cdot]$  be the floor function) will have a Chern number  $C_l = -1$ . Thus, this choice provides us a way to explore situations with different topological invariants  $t_l$  just by probing different energies. Note that other fluxes can lead to different Chern number combinations. For example, as we will see below,  $\phi = 4/9$  leads to a lowest energy band with  $C_0 = 2$ , and  $\phi = 5/14$  leads to  $C_0 = 3$ . Due to the bulk-boundary correspondence, these quantized topological invariant will have important consequences when we consider open boundary conditions, as they will give rise to a number of localized, gapless edge states. To illustrate that, we consider now the system to be placed in a cylinder geometry, such that the system is periodic in the  $Y$  direction but open in the  $X$  direction, defining two edges where localized states can appear. To confirm that localized edge states appear, we plot in Fig. 5(b) the spectrum of the system as function of  $k_y$ , which is still a good quantum number, for the same parameters as in Fig. 5(a). There, we observe how, on top of the flat bands appearing in the bulk modes, several-edge-mode dispersion appears associated with each of the lowest Landau-levels. This means that the larger the energy of the band gap is, the larger the number of edge states. To further characterize the properties of the edge modes appearing in such band gaps, let us note that the eigenmodes in these configurations can be written as  $H_B|k_y, \beta\rangle = E_\beta(k_y)|k_y, \beta\rangle$ . Projecting their wave function into their spatial coordinates  $\langle x, y|\Psi_{\beta, k_y}\rangle = e^{ik_y y} \psi_{\beta, k_y}(x)$ , one can find that  $\psi_{\beta, k_y}(x)$  satisfies the Harper equation,

$$\begin{aligned} \psi_{\beta, k_y}(x+1) + \psi_{\beta, k_y}(x-1) + 2 \cos(2\pi\phi x - k_y) \psi_{\beta, k_y} \\ = E_\beta(k_y) \psi_{\beta, k_y}(x), \end{aligned} \quad (\text{A7})$$

and it features a localized shape. To make it more evident, we define a localization parameter for each eigenstate as follows:

$$\eta = \sum_{x=0}^{L-1} \left( -1 + 2 \frac{x}{Lx-1} \right) |\psi_{\beta, k_y}(x)|^2, \quad (\text{A8})$$

which features a maximum  $\pm 1$  value when localized in the left/right edge, and 0 when it is delocalized. We codify the value of that parameter in Fig. 5(a) in a color scale where purple/yellow indicates a maximum localization in the left/right edges, whereas blue indicates delocalization. There, we observe another important property of the edge states: The modes along one edge are perfectly chiral, since they feature a positive/negative group velocity depending on the edge where they are localized. This will have important consequences when an emitter couples to one of the edges, as we will see in Appendix C.

## APPENDIX B: EFFECTIVE EDGE MODE DESCRIPTION AS A MULTIMODE WAVEGUIDE

As shown in Fig. 5(b), the first band gaps of the HH can host a controllable increasing number of edge modes. Since these are effectively one-dimensional modes and are chiral, they can be seen as an effective multimode one-way waveguide [37,38]. Generally, such topological modes have been described within linear approximations [26–28]. However, from Fig. 5 it is clear that this is not the case in this scenario. In what follows, we will derive a more accurate effective theory that is able to analytically capture the behavior of these multimode wave guides. For concreteness, we will derive such expressions for the left-localized edge states, although a similar description can be found for the right-localized ones.

### 1. Situation with $\phi = 1/q$

Let us start with the situation  $\phi = 1/q$  that we consider in the main text and in Fig. 5. After extensive numerical analysis, we find that a good empirical ansatz for the  $l$ th eigenmode dispersion for small magnetic fluxes is given by

$$\omega_{\text{eff}, l}(k_y) = \omega_l(\phi) + a_l(\phi)[k_y - k_l(\phi, L)]^2, \quad (\text{B1})$$

where  $\omega_l(\phi)$  can be found approximately in the perturbative limit [60] as

$$\begin{aligned} \frac{\omega_l(\phi)}{J} = -4 + 2\pi\phi \left( l + \frac{1}{2} \right) - (\pi\phi)^2 \left( l^2 + l + \frac{1}{2} \right) \\ + \mathcal{O}(\phi^3), \end{aligned} \quad (\text{B2})$$

whereas  $a_l(\phi)$  and  $k_l(\phi, L)$  are fitting parameters that depend on both the effective flux  $\phi$  and  $l$ th edge mode considered, although not on system size as long as  $l_B \ll L$ . Note such quadratic energy dispersions are typical of other (topologically trivial) waveguides, where the finite size effects introduce energy cutoffs for the modes that lead to that behavior. To further characterize this effective model, we start plotting in Fig. 6(a) the evolution of the curvature of the edge modes,  $a_l(\phi)$ , as a function of  $\phi$  for the three lowest-energy edge modes in different colors. There, we see how for big fluxes  $\phi$  the curvatures of the modes differ significantly, whereas for small fluxes, they converge to a value  $a_l(\phi) \approx 0.6$ . Regarding the value of the momentum cut-off  $k_l(\phi, L)$ , we find that there is a linear dependence with  $\omega_l(\phi)$ , i.e.,  $k_l(\phi) = \beta_l \omega_l(\phi) \pmod{2\pi}$ . To illustrate that, in Fig. 6(b) we plot them for several fluxes in the range  $\phi \in [\frac{1}{60}, \frac{1}{12}]$ , with dotted lines indicating the result of the fitting. To discuss the dependence of  $k_l$  on the system size  $L$ , we may rewrite Eq. (A7) as

$$\psi_{\beta, k_y}(x+1) + \psi_{\beta, k_y}(x-1) + V_\phi(x) = E_\beta(k_y) \psi_{\beta, k_y}(x), \quad (\text{B3})$$

where the potential  $V_\phi(x)$  is given by

$$V_\phi(x) = 2 \cos(2\pi x \phi - k_y), \quad x = 0, 1, \dots, L-1. \quad (\text{B4})$$

We observe that varying  $L$  modifies the boundary condition of the Harper equation in the right edge. However, if  $\phi = 1/q$  and  $L$  is increased or decreased in  $nq$  sites ( $n \in \mathbb{N}$ ), the boundary condition remains, leading to  $k_l(\phi, L) - k_l(\phi, L') = 2\pi\phi(L - L')$ . In Fig. 7(a), we show the comparison between

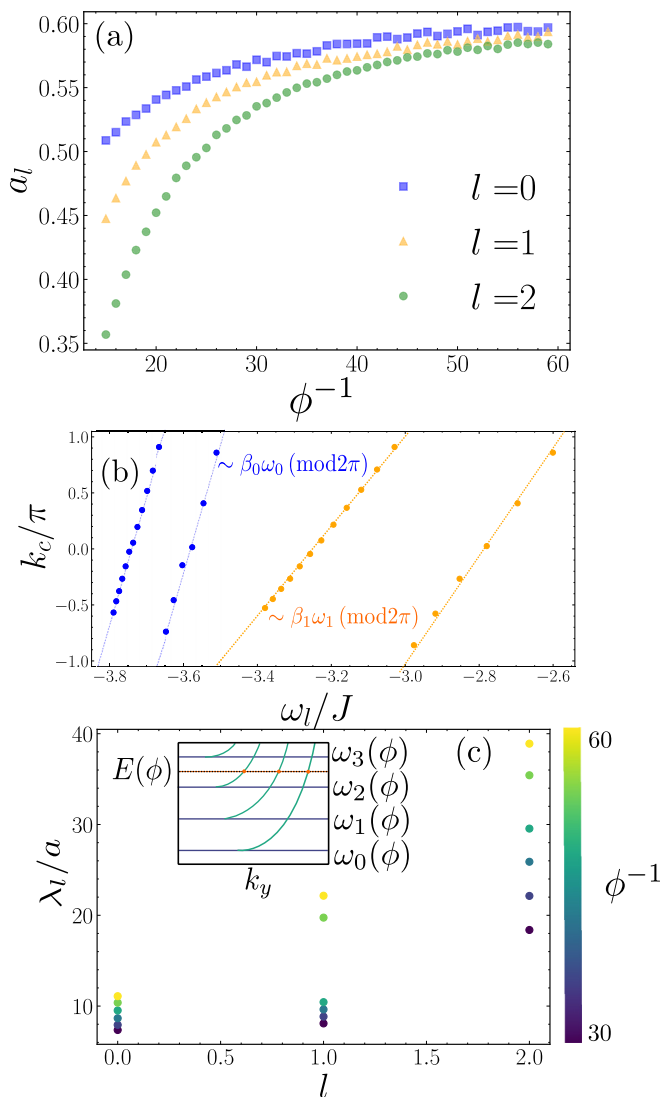


FIG. 6. (a) Fitted values of the effective model parameter  $a_l(\phi)$  in Eq. (B1), characterizing the curvature of the edge-mode dispersion for the three lowest-energy edge states. In the limit of small fluxes,  $\phi \rightarrow 0$ , all curvatures tend to the same value  $\sim 0.6$ . (b) Fitted values of  $k_l$  as a function of the Landau level energy  $\omega_l$ , for different magnetic fluxes  $\phi = 1/q$  ranging from  $q = 12$  to  $q = 60$ . We observe a linear trend  $k_l = \beta_l \omega_l \pmod{2\pi}$ . Note that the discontinuity between the lines occurs because of the definition of  $k_l(\pi)$  over the  $[-\pi, \pi]$  range. Both panels (a) and (b) are obtained considering a HH lattice of  $40 \times 40$  sites. (c) Localization length  $\lambda_l$  of the three lowest edge modes for different values of  $\phi$ , encoded in the markers' color. All localization lengths are computed at the same energy, namely the middle of the third spectral band gap, as depicted in the figure inset.

the exact diagonalization results and our effective description for a particular value of  $\phi$ , showing indeed an excellent agreement for the lowest edge-state dispersions. In Fig. 7(b), we make a more quantitative assessment of the quality of the model by defining an error parameter:

$$\varepsilon_l = \frac{1}{N_k} \sum_{k_y \in \Omega} |\omega_{\text{exact},l}(k_y) - \omega_{\text{eff},l}(k_y)|^2, \quad (\text{B5})$$

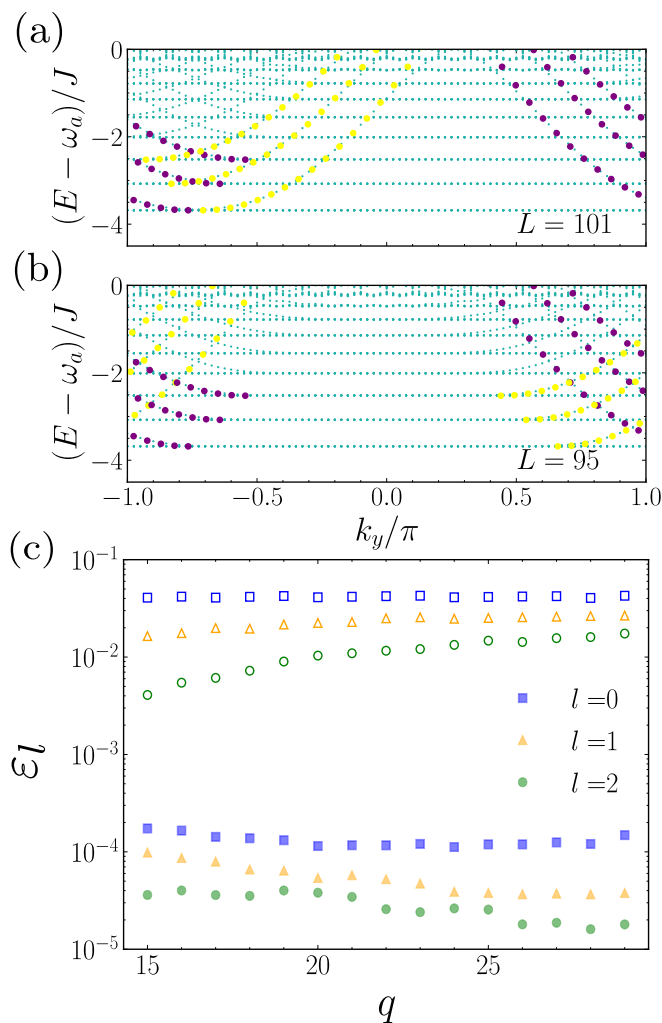


FIG. 7. (a), (b) Effective model vs exact diagonalization for a magnetic flux  $\phi = 1/19$  and two different system sizes. In both panels, blue dots represent the bath spectrum obtained by exact diagonalization. Purple/yellow dots represent the prediction of the effective model of the energies of edge modes localized at the left/right edge. Notice that with varying  $L$ , the dispersion relation of right-localized states is shifted along  $k_y$ , which can also be captured by the effective model, although we did not explicitly show that. (c) Fitting error, as defined in Eq. (B5), for the three lowest edge modes and varying flux. Empty and filled markers correspond to linear and quadratic fittings respectively. We observe that, for all cases, the quadratic fit error is few order of magnitudes lower, showing that this approach is significantly more realistic.

where  $\Omega$  is some region in the Brillouin zone along  $Y$  where we are interested in performing the approximation to the exactly numerically calculated edge-mode dispersion,  $\omega_{\text{exact},l}(k_y)$ , and  $N_k = |\Omega|$  is the number  $k_y$  of modes within that region. In Fig. 7(b), we plot  $\varepsilon_l$  as a function of  $\phi$  and compare the accuracy between a linear fit, i.e.,  $\omega_{\text{eff},l}(k_y) \propto k_y$  (empty markers) and the quadratic fit of Eq. (B1) (filled markers), showing how indeed the later provides a much more accurate approximation of the modes for all fluxes. Apart from the energies, another magnitude of the modes of interest is the localization parameter. In particular, we know from



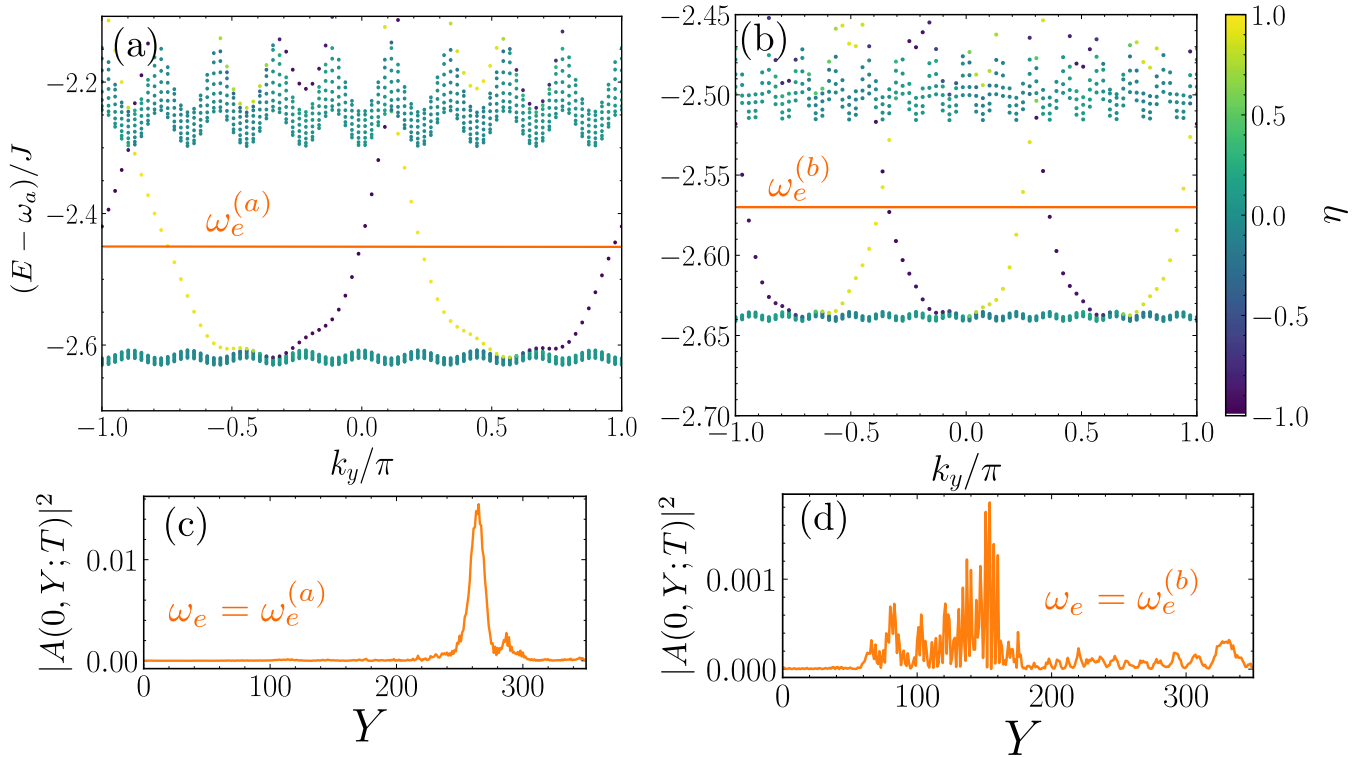


FIG. 8. (a), (b) Lowest energy spectrum of a Harper-Hofstadter lattice of  $80 \times 80$  sites with a magnetic flux of (a)  $\phi = 4/9$  and (b)  $\phi = 5/14$ . In each case, the lowest band has a Chern number of 2 and 3 respectively, which correspond to the number of edge modes per boundary resonant to the lowest spectral band gap. (c), (d) Snapshots of the photonic dynamics at time  $TJ = 300$  of spontaneous emission along the  $Y$  axis of an emitter coupled to the left boundary of the lattice with coupling  $g/J = 0.2$ . The frequency of the emitter in each case is indicated in the (a) and (b) plots as a solid orange line, and is  $\omega_e^{(a)}/J = -2.45$  and  $\omega_e^{(b)}/J = -2.57$ . We can observe that the pulse shape differs from the single mode scenario. However, it is not possible in this case to resolve the different peaks of the pulse due to the similarity of the group velocities of the different topological channels.

Eq. (A7) that when  $E_\beta(k_y)$  lies within a band gap the spatial wave function along  $X$  will be exponentially localized, i.e.,  $\psi_\beta(x) = \sqrt{2/\lambda_l(\phi)}e^{-x/\lambda_l(\phi)}$ , where  $\lambda_l(\phi)$  will depend on both the energy level  $l$  and the flux  $\phi$ . In Fig. 6(c) we also plot its dependence, showing that higher-energy edge modes are less localized, and also that increasing the value of  $\phi$  yields to higher delocalization.

## 2. Other situations $\phi \neq 1/q, q \in \mathbb{N}$

In this work, we have considered magnetic fluxes of the form  $\phi = 1/q$ , with  $q \in \mathbb{N}$ , due to the emergence of  $[q/2]$  lowest bands with Chern number  $C = 1$ . This structure does not prevail if  $\phi$  does not fit this form. To illustrate this, we consider the cases of  $\phi = 4/9$  and  $5/14$  in Figs. 8(a), 8(c) and Figs. 8(b), 8(d), which feature Chern numbers of  $C_0 = 2, 3$ , respectively. We start by plotting the spectrum for such values of  $\phi$  in panels (a) and (b), where we see that the lowest band gap features four and six edge-state dispersions, respectively, as expected from the value of  $C_0$ . In general, through numerical inspection we found that in these situations the energy dispersions of the modes tend to be more similar than in the different band gaps of the  $\phi = 1/q$  situation. This will result in qualitatively different spontaneous emission patterns, as observed in panels (c) and (d), where we plot snapshots of the emission in two different situations, illustrating the richness

of this setup to obtain qualitatively different photonic wave packets.

## APPENDIX C: SPONTANEOUS EMISSION OF EMITTERS COUPLED TO THE EDGE OF THE PHOTONIC LATTICE

In this section, we will consider what happens when a two-level emitter, with Hamiltonian  $H_S = \omega_e \sigma_{ee}$ , couples to one of the edges of a HH lattice that, for concreteness, we assume to be the left one of Fig. 1(a) of the main text. In general, we will consider the most standard local light-matter couplings given by

$$H_I = g \sigma_{eg} a_{\mathbf{r}_e} + \text{H.c.}, \quad (\text{C1})$$

where  $g$  is the coupling strength of the bath,  $\mathbf{r}_e$  the position of the cavity mode the emitter couples to, and  $\sigma_{\alpha\beta} = |\alpha\rangle\langle\beta|$  the dipole operator of the optical emitter transition that couples the photonic bath. In Appendix C6, however, we will consider the nonlocal couplings that can be engineered with giant atoms [53–57], as a way of selectively coupling some of the topological edge modes.

### 1. Expected Markovian decay rates or local density of states

A single emitter can be prepared in its excited state with a classical driving, e.g., using a  $\pi$  pulse. If one assumes that

the bath has initially no excitations, this state,  $|\Psi_0\rangle = |e\rangle \otimes |\text{vac}\rangle_B$ , can only evolve into an state of the form

$$|\Psi(t)\rangle = \left( C_e(t)\sigma_{eg} + \sum_{\mathbf{r}} A_{\mathbf{r}}(t)a_{\mathbf{r}}^\dagger \right) |g\rangle \otimes |\text{vac}\rangle_B, \quad (\text{C2})$$

because the full light-matter Hamiltonian,  $H = H_S + H_B + H_I$ , conserves the number of excitations  $N_{\text{exc}} = \sigma_{ee} + \sum_{\mathbf{r}} a_{\mathbf{r}}^\dagger a_{\mathbf{r}}$  since  $[H, N_{\text{exc}}] = 0$ . Using time-dependent perturbation theory or, equivalently, a Markovian approximation for the system-bath coupling, the emitter is expected to show an exponential decay of its excitation, i.e.,  $|C_e(t)|^2 \approx e^{-\Gamma t}$ , with  $\Gamma$  being the expected Markovian decay rate given by Fermi's Golden rule [106]:

$$\begin{aligned} \Gamma(\omega_e) &= 2\pi g^2 \sum_{\beta} |\psi_{\beta}(0)|^2 \delta(\omega_e - E_{\beta}(k_y)) \\ &= -2g^2 \text{Im} \left[ \frac{1}{\omega_e + i0^+ - H_B} \right]_{\mathbf{r}_e, \mathbf{r}_e} \\ &= 2g^2 \text{LDoS}(\mathbf{r}_e, \omega_e). \end{aligned} \quad (\text{C3})$$

In the last equality we introduced the local density of states (LDoS) at the emitter position. This quantity is defined similarly to the regular DoS, but weighting the contribution of each bath eigenstate by its support on the position of the emitter:

$$\text{LDoS}(\mathbf{r}, E) = \sum_{E_B} |\langle \mathbf{r} | E_B \rangle|^2 \delta(E - E_B) \quad (\text{C4})$$

From this definition, the relation of the LDoS with the Markovian decay rate becomes clear by comparing with Eq. (3) of the main text, since

$$\begin{aligned} |\langle e | H_I | E_B \rangle|^2 &= |\langle e | g \sigma_{eg} a_{\mathbf{r}_e} | E_B \rangle|^2 \\ &= g^2 |\langle 0 | a_{\mathbf{r}_e} | E_B \rangle|^2 = g^2 |\langle \mathbf{r}_e | E_B \rangle|^2, \end{aligned} \quad (\text{C5})$$

where  $|0\rangle = |g\rangle |\text{vac}\rangle$ . We numerically compute the LDoS in a similar fashion as we did for the DoS, defining a ‘‘smoothed’’ Dirac delta function  $f_{\theta}(E - E_B)$ , that we take to be a Gaussian distribution as expressed in Eq. (A5), and computing the LDoS as

$$\text{LDoS}(\mathbf{r}_e, E) \approx \sum_{E_B} |\langle \mathbf{r}_e | E_B \rangle|^2 f_{\theta}(E - E_B), \quad (\text{C6})$$

From Eq. (C3) we read that the shape of the LDoS determines the shape of the expected Markovian decay rate  $\Gamma(\omega_e)$ . In Fig. 9(a) we plot the Markovian decay rate at the emitter position calculated with exact diagonalization, for several values of  $\phi$ . We observe that smaller  $\phi$ 's are associated with narrow band gaps, a situation in which the LDoS ‘‘quasiquantized’’ behavior leads to plateaus in  $\Gamma(\omega_e)$ . In Fig. 9(b), we represent with a solid line the expected decay rate  $\Gamma_e$  as a function of  $\omega_e$  for  $\phi = 1/12$ , computed using exact diagonalization, and compare it with the markers that represent the expected decay rate computed as follows:

$$\Gamma_l(\omega_e) \approx \frac{g^2 |\psi_l(0)|^2}{|v_{g,l}(\omega_e)|} = \frac{2g^2}{\lambda_l |v_{g,l}(\omega_e)|}, \quad (\text{C7})$$

where  $v_{l,g}(\omega_e)$  is the group velocity of the  $l$ th mode at the emitter energy, that is,  $v_{g,l} = \partial_{k_y} \omega_{\text{eff},l}(k_y)|_{k_y=k_e}$ , with

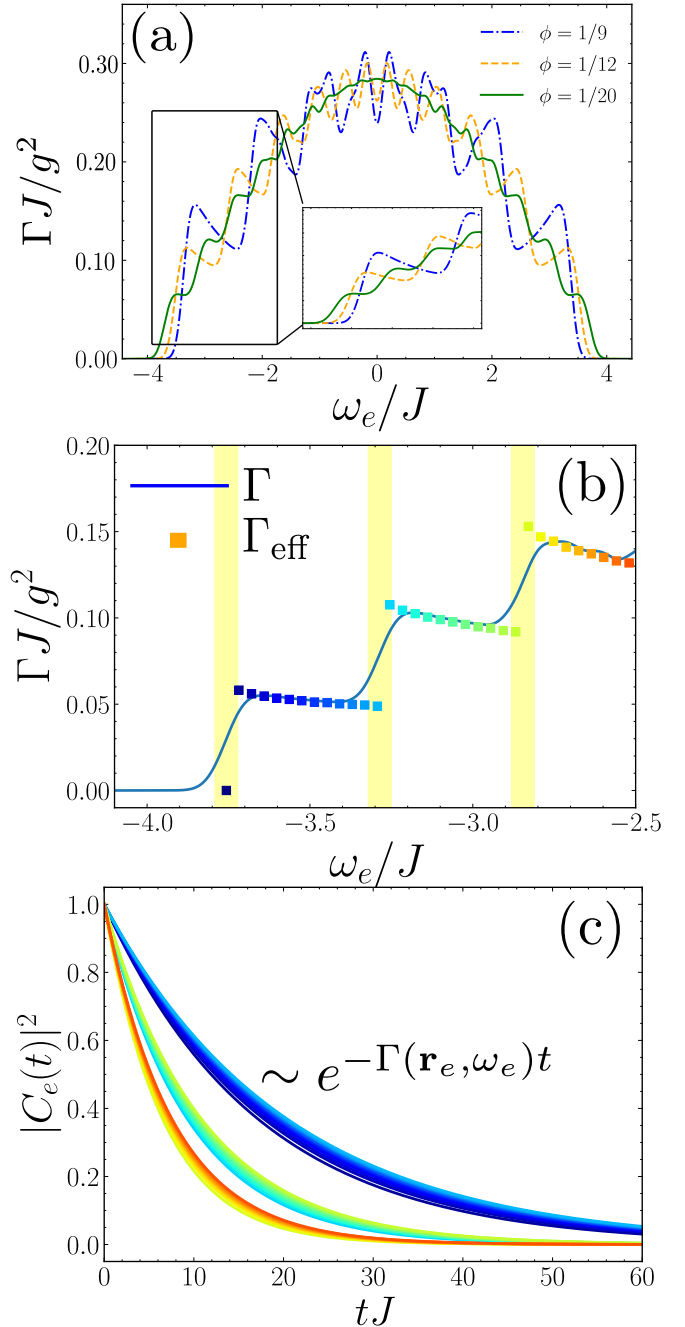


FIG. 9. (a) Markovian decay rate of a quantum emitter coupled to the edge of a HH lattice of  $100 \times 100$  sites, for different values of the magnetic flux  $\phi$ , and computed by exact diagonalization [computed using an auxiliary width of  $\theta/J = 0.15$  as defined in Eq. (A5)]. The decay rate curves in the lowest part of the spectrum are zoomed in the figure, showing that lower fluxes support more constant plateaus in the spectral band gaps. (b) For the same lattice size, the Markovian decay rate for  $\phi = 1/25$  is depicted as a solid line. Square markers depict the prediction of our effective model for the decay rate in this specific configuration. (c) Spontaneous decay of the emitter population in the same configuration as in (b) for different values of  $\omega_e$  and  $g/J = 0.05$ . Each curve is linked to a value of  $\omega_e$  and its corresponding color is depicted by the square markers in (b).

$\omega_{\text{eff},l}(k_e) = \omega_e$ . Thus, the total decay rate in a given band gap will be given by  $\Gamma(\omega_e) = \sum_l \Gamma_l(\omega_e)$ , where the sum runs over the number of edge modes that are present in that band gap. We observe that the decay rate displays a ladderlike structure, with jumps located at Landau levels. This quasiquantization behavior can be probed by monitoring the decay of the emitter population during spontaneous emission. In Fig. 9(c) we show the quantum emitter dynamics of an initially excited emitter for the range of  $\omega_e$  depicted in Fig. 9(b). There, we observe how its timescale remains approximately constant until it crosses the Landau level energy and is able to interact with the new mode of the higher band gap. We note, however, that the steps of the ladder are not strictly constant due to the nonlinear dependence of the mode dispersion. On the contrary, they display the typical  $1/\sqrt{\omega - \omega_{\text{edge}}}$  dependence associated with one-dimensional quadratic band-edge dispersions. For the lowest-energy edge modes, we observe agreement between the our analytical model and the numerical calculations, except near the Landau level divergences. At these energies the numerical computation of the LDoS entails limited resolution, due to the finite width  $\theta$  associated with the auxiliary function  $f_\theta(E - E_B)$ : If we probe the LDoS of an energy  $|E - \omega_l| < \theta$  from below, the LDoS will count some states above  $\omega_l$ , softening the transition. This issue is unavoidable: if we try to have an arbitrarily small value of  $\theta$ , the probe function will eventually observe the discreteness of the spectrum. In such case, the computation of the LDoS would suffer from numerical instabilities. In contrast, an excessively large value for  $\theta$  will make the approximation states in Eq. (C6) increasingly worse. In our case, the information about the LDoS jumps would be lost, softening the shape of the curve. All these numerical issues are graphically represented in Fig. 10.

## 2. Photonic spontaneous emission patterns

As we see in Fig. 3 of the main text, the nonuniform group velocity of the modes along a given band gap favours a spatial separation of the photons propagating into the different channels. This generates naturally single-photon time-bin entangled states [65], that when combined with sequential generation methods [52,68–83] can be used to generate complex states of light in these topologically protected channels. Let us now analyze here the relevant magnitudes that determine such spontaneous separation of the photons, focusing on the second band gap where there are two edge modes. If we neglect the broadening introduced by the nonlinear mode dispersion, which we will see below is a good approximation in our system, the spatial separation between the different modes is determined by

(i) The different group velocities,  $v_{g,l}$ , which yield that after a time  $T$  the wave-packet fronts are separated by  $|v_{g,l} - v_{g,l'}|T$ . With our choice of units, that length is already normalized to lattice constant units.

(ii) The spatial broadening of the modes, which are of the order of  $1/\Gamma_l^{-1}$  in lattice constant units [107].

Thus, one can define a parameter  $R_{l,l'}$ ,

$$R_{l,l'} = \frac{|v_{g,l} - v_{g,l'}|}{\Gamma_l^{-1} + \Gamma_{l'}^{-1}}. \quad (\text{C8})$$

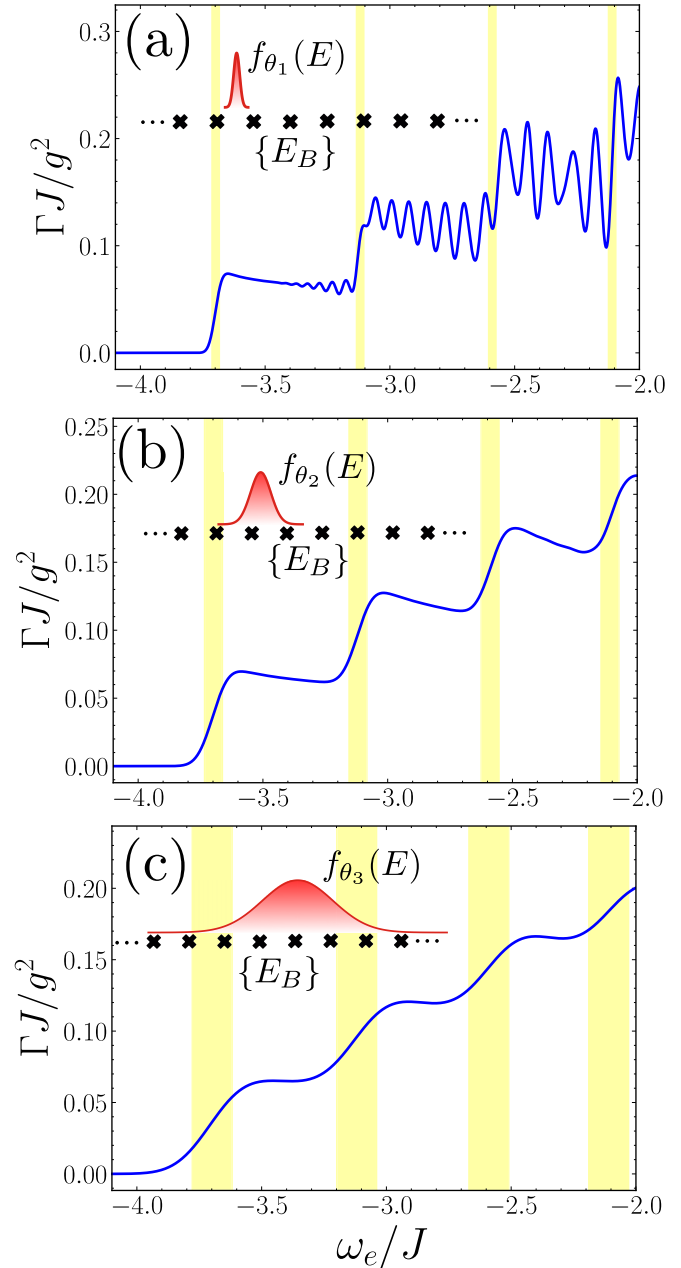


FIG. 10. Markovian decay rate from exact diagonalization at the boundary of a HH lattice of size  $120 \times 120$  and  $\phi = 1/15$ . The figures are obtained using an auxiliary function width of (a)  $\theta_1/J = 0.03$ , (b)  $\theta_2/J = 0.07$ , and (c)  $\theta_3/J = 0.16$ . The figure insets represent as crossed markers the distribution of bath eigenvalues  $\{E_B\}$ . Above these markers, we include a representation of the auxiliary probe Gaussian function  $f_\theta(E - E_B)$  that is used as described in Eq. (C6) to probe the energy spectrum and compute the LDoS. In each figure, the vertical yellow fringes are centered at Landau levels, and their width is equal to the corresponding value of  $\theta$ .

which quantifies how favorable is a given configuration to observe the separation of the modes. This quantity has dimensions of energy (i.e., inverse time) and captures the competition between the spatial broadening  $\propto \Gamma_l^{-1} + \Gamma_{l'}^{-1}$  and the pulse separation induced by the difference between group velocities  $|v_{g,l} - v_{g,l'}|$ . When  $R_{l,l'}T \sim 1$ , it is expected that the

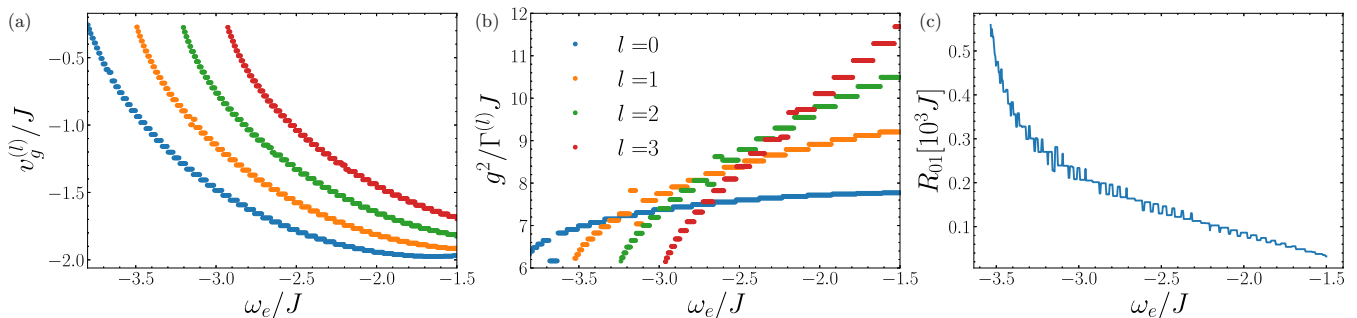


FIG. 11. (a) Group velocities of the lowest four edge modes of a HH lattice of  $50 \times 50$  sites and  $\phi = 1/40$ . (b) Inverse decay rate  $1/\Gamma^{(l)}$  of the quantum emitter onto each topological channel  $l$ , in units of  $J/g^2$ , and for the case of  $g/J = 0.1$ . (c) Distinguishability parameter  $R_{0,1}$ , as defined in Eq. (C8), for the two lowest edge modes in the  $\phi = 1/40$  configuration.

modes  $l$  and  $l'$  are fully resolvable at time  $T$ . In Fig. 11 we plot the different group velocities of the modes [panel (a)], broadenings [panel (b)], and  $R_{0,1}$  [panel (c)] as a function of the quantum emitter energy  $\omega_e$  for a given bath configuration with  $\phi = 1/40$ . From Fig. 11(c) we observe that the pulses associated with modes 0 and 1 will be fully resolvable at  $TJ \sim 10^3$ . As expected, the best conditions to achieve resolution will occur when the quantum emitter energy  $\omega_e$  is slightly above the Landau level energy  $\omega_1$ ; in this case,  $|v_{g,0} - v_{g,1}|$  will be maximum, which favors resolution. Apart from the intrinsic broadening of the emitted wave packets, let us also note that there is an additional source of broadening coming from the curvature of the edge-mode dispersion at the emitter's frequency, that is,  $\gamma_{\text{dis}}$  in  $\omega_l(k) \approx \omega_e + v_{g,l}(k - k_e) + \gamma_{\text{dis}}(k - k_e)^2/2$ . In particular, it is well known that a wave packet with an initial broadening  $\sigma_0$  propagating in such a nonlinear dispersive channel will have an increasing size growing with

$$\sigma(t) = \sigma_0 \sqrt{1 + \frac{\gamma_{\text{dis}}^2 t^2}{\sigma_0^4}}. \quad (\text{C9})$$

In the case of spontaneous emission of a quantum emitter into the  $l$ th topological channel of a HH lattice, we can take  $\sigma_0$  as the inverse of the decay rate to such mode,  $\Gamma_l^{-1}$ . The pulse width will then evolve as

$$\sigma(t) \sim \frac{1}{\Gamma_l} \sqrt{1 + \gamma_{\text{dis}}^2 \Gamma_l^4 t^2}. \quad (\text{C10})$$

From this evolution equation, it follows that the role of dispersion will be negligible at a certain time  $T$  as long as

$$\gamma_{\text{dis}}^2 \Gamma_l^4 T^2 \ll 1 \quad (\text{C11})$$

Taking  $g/J \sim 0.1$ , we find that  $\Gamma_l/J \sim 10^{-3}$ . On the other hand, we can estimate  $\gamma_{\text{dis}}$  from our effective theory; in particular, we will have that  $\gamma_{\text{dis}} \sim 2a_l(\phi)[k_y - k_l(\phi)]$ , which will be at most of the order of the unity. Thus, at this value of  $g$ , dispersion effects will be thus relevant at times  $TJ \sim 10^6$ , which is several orders of magnitude above the timescale where the pulses are separable due to different group velocities, characterized by  $R_{ll'}T \sim 1$ .

### 3. Robustness to disorder

In Figs. 3(a), 3(c), and 3(e) of the main text, we have shown the robustness of single-, two-, and three-edge-mode propagation to an edge defect. This is a consequence of the topological nature of the edge modes. Here, we discuss in greater detail the protection of photon propagation against disorder by introducing random perturbations in the energy of local lattice modes, as follows:

$$H \rightarrow H + \sum_{\mathbf{r}} \delta\omega_{\mathbf{r}} a_{\mathbf{r}}^{\dagger} a_{\mathbf{r}}, \quad (\text{C12})$$

where  $\delta\omega_{\mathbf{r}}$  is a random variable uniformly distributed along the interval  $(-\sigma, \sigma)$ , where  $\sigma$  is the strength of the applied disorder. Topological gapless modes spectrally located at a band gap of width  $E_W$  are typically expected to be robust to disorder strengths  $\sigma$  up to the order of  $E_W$ . In Fig. 12, we first analyze the effect of disorder qualitatively in two key features: The LDoS defined in Eq. (C4) and photon emission and propagation. In Fig. 12(a) we plot the Markovian decay rate, computed from exact diagonalization, for an emitter coupled at the boundary of a HH lattice for  $\phi = 1/12$  for different values of  $\sigma$  averaged among different realizations of disorder. We observe that the ladder structure is preserved for values of  $\sigma$  comparable to the width of the lowest spectral band gaps. This is a consequence of the protection of the multimode spectrum in the topological band-gaps. Furthermore, in Figs. 12(b)–12(d), we plot photon population emitted for an emitter resonant to the second lowest band gap of the bath spectrum and for different values of  $\sigma$ . For weak disorder, i.e., small  $\sigma$  compared to  $E_W$ , we observe the same light-cone configuration as in the  $\sigma = 0$  case. We only start to witness light-cone distortion for values of  $\sigma$  comparable to the size of the band gap that is resonant to the emitter energy. Now, let us make a more quantitative description of the impact of disorder in the propagation of the edge modes in such a multimode scenario. For that, we use the method proposed in Ref. [91], where they quantify the robustness of photon transport by partitioning the Hilbert space into bulk and edge modes and by observing the edge mode content of the photonic state when defects or local disorder are present. To distinguish between edge and bulk modes of the spectrum, we compute the localization properties of each eigenstate of the system



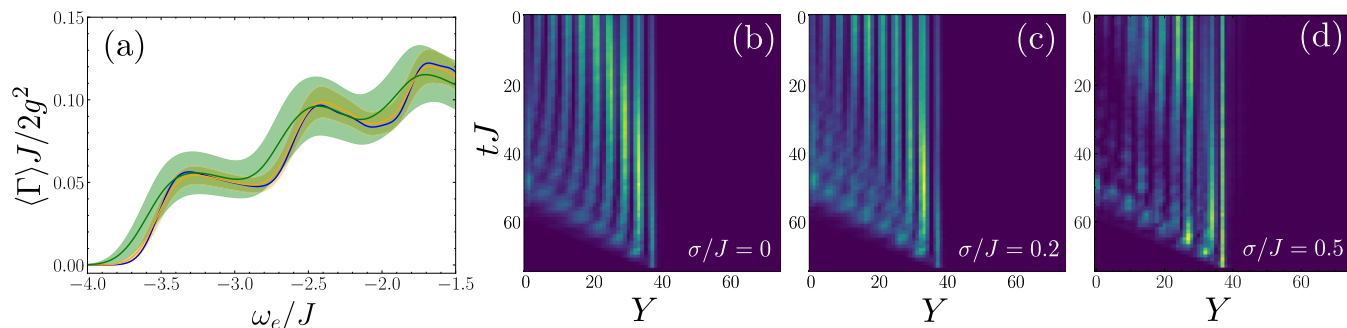


FIG. 12. (a) Ensemble average of the Markovian decay rate of a quantum emitter coupled at the boundary of a HH lattice of  $30 \times 30$  sites for  $\phi = 1/12$  for different values of disorder strength:  $\sigma/J = 0$  (blue),  $\sigma/J = 0.35$  (orange), and  $\sigma/J = 0.7$  (green). Each solid line represent the mean LDoS for a collection of 100 realizations of disorder, whose variance is represented as a shaded region around the mean. Every curve is computed by exact diagonalization, using an auxiliary width of  $\theta/J = 0.15$  as defined in Eq. (A5). (b), (c), (d) Photon transport from the spontaneous emission of such a quantum emitter with energy  $\omega_e/J = -2.48$  along the left boundary of a HH lattice of  $70 \times 70$  sites and  $\phi = 1/12$ , for several values of disorder strength. We observe that photon transport is robust for small values of  $\sigma$ . The effects of disorder only start to arise for  $\sigma \sim 0.5J$ , which is of the order of the band-gap width  $E_W \sim 0.77J$ .

using the inverse participation ratio (IPR), defined as follows:

$$\text{IPR}(\Psi) = \frac{1}{\sum_{\mathbf{r}} |\Psi_{\mathbf{r}}|^4} \quad (\text{C13})$$

If a wave function is spread in a discrete space of  $N$  sites, its IPR will be of the order of  $N$ . Then, we would expect an IPR of the order of  $L^2$  for bulk modes (which spread along the whole lattice) and of  $L$  for edge states (which are localized along one dimension). In Fig. 13(a) we observe these expected scaling relations. The implication of this is that larger lattices lead to larger distinction of the IPR of the bulk and edge modes, thus allowing a clear bipartition by considering a given threshold  $\varepsilon$  in the IPR. After defining the partition of the Hilbert space, we quantify the edge mode content as the associated norm of the emitted wave function at a certain time,

$|\psi_{\text{ph}}\rangle$ , projected into the edge-mode subspace:

$$\mathcal{E}(\psi_{\text{ph}}) = \sum_{\text{IPR}(\Psi) < \varepsilon} |\langle \Psi | \psi_{\text{ph}} \rangle|^2, \quad (\text{C14})$$

where the sum is performed over all lattice eigenstates  $|\Psi\rangle$  whose IPR is below a given threshold. In Fig. 13(b) we consider a single square defect of increasing size  $|\mathcal{D}|$ , and study how much the excitation spreads out of the edge modes after impinging with it. We compare the situation with two different system sizes and find that the edge mode content in both cases is practically constant. Furthermore, we see that this robustness measure is higher for larger lattices, where the protection of the edge modes is better. In the inset, we represent a snapshot of the spontaneous emission dynamics where we see that transport is highly protected even for large defects. On top of that, we also consider a different disorder

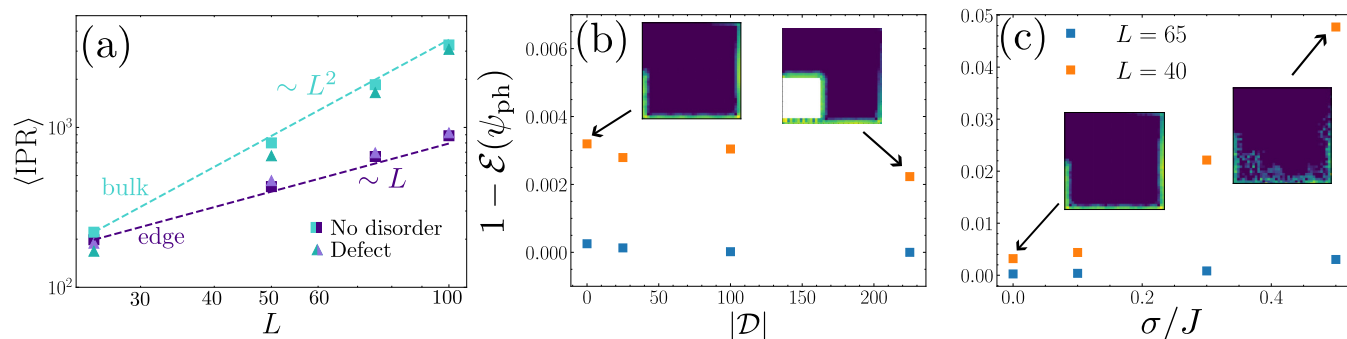


FIG. 13. (a) Scaling with lattice size  $L$  of the inverse participation ratio (IPR) for bulk and edge states in presence vs absence of defects. The magnetic flux is  $\phi = 1/9$ . The IPR of edge states is computed as the average of all lattice eigenstates with an energy in the lowest spectral band gap, while bulk states IPR is calculated as an average of eigenstates with an energy equal to the second Landau level. The considered defect has a size of  $10 \times 10$  sites. (b), (c) Effect of disorder induced by defects (b) and local energy perturbations (c) in the edge mode content  $\mathcal{E}$  of the spontaneously emitted photon, for two different lattice sizes. In both cases, we plot  $1 - \mathcal{E}$  (which can be interpreted as the bulk mode content) for two different lattice sizes and varying defect sizes and disorder strengths. In both cases, the photonic state is obtained from spontaneous emission of an atom with frequency  $\omega_e \approx -2.79J$  and coupled to the lattice with a coupling strength  $g = 0.05J$ , and evaluated at time  $T = 100/J$ . For  $L = 40$  ( $L = 65$ ), the bulk-edge IPR threshold is set to 500 (800). The insets depict snapshots of the spontaneous emission dynamics of an emitter coupled to the center of the left edge, for a lattice size of  $L = 40$ .

situation, that is, a random energy disorder over the lattice sites with a normal distribution of width  $\sigma$  [see Fig. 13(c)]. In this case, we find it more instructive to project directly to the edge-mode subspace of the clean system, since bulk modes undergo Anderson localization, and hence the IPR is no longer valid to differentiate bulk and edge states. In Eq. (C14), this implies doing the sum over the edge eigenstates  $|\Psi\rangle$  of the pristine Hamiltonian. In this case, we see that the edge-mode content decreases for higher disorder strengths, revealing lack of protection for values of  $\sigma$  of the order of  $\omega_e - \omega_{\text{bulk}}$ , which is  $\approx 0.57J$  in the situation represented in the figure. Again, we also observe that larger sizes favor protection.

#### 4. Photon-loss effects

In this paper, we have neglected the possibility that the emitter or bath mode couples to another additional bath, generating additional decay rates. In that case, the emitter-bath dynamics must be described by a density matrix,  $\rho(t)$ , formalism. Assuming that the couplings to these baths are Markovian, the dynamics of such a density matrix can be described by the following time-local master equation:

$$\begin{aligned} \frac{\partial \rho}{\partial t} = & i[\rho, H] + \sum_{\mathbf{r}} \frac{\kappa_{\mathbf{r}}}{2} (2a_{\mathbf{r}}\rho a_{\mathbf{r}}^{\dagger} - a_{\mathbf{r}}^{\dagger}a_{\mathbf{r}}\rho - \rho a_{\mathbf{r}}^{\dagger}a_{\mathbf{r}}) \\ & + \frac{\Gamma^*}{2} (2\sigma_{ge}\rho\sigma_{eg} - \sigma_{ee}\rho - \rho\sigma_{ee}), \end{aligned} \quad (\text{C15})$$

where  $\kappa_{\mathbf{r}}$  and  $\Gamma^*$  are the Markovian decay rates induced by these additional baths in the bath and emitter modes, respectively. In the spontaneous emission configuration that we have considered in this paper, all the effect of these baths can be captured by replacing the full light-matter Hamiltonian  $H$  by a non-Hermitian version which includes the effect of the losses:

$$H^* = H_S + H_B + H_l - i \sum_{\mathbf{r}} \frac{\kappa_{\mathbf{r}}}{2} a_{\mathbf{r}}^{\dagger} a_{\mathbf{r}} - i \frac{\Gamma^*}{2} \sigma_{ee}. \quad (\text{C16})$$

In Fig. 14(a), we plot its effect in the predicted Markovian decay rates for increasing values of  $\kappa_{\mathbf{r}} = \kappa$  and fixing  $\Gamma^*$ . There, we observe a “softening” of the steps of the ladder, although the quasiquantized behavior remains unaltered to a great extent. A similar behavior will occur with  $\Gamma^* \neq 0$ . The most significant effect of  $\kappa$  is to generate a finite propagation length of the photon modes, as observed in Figs. 14(b) and 14(c), where we plot an example of the spontaneously emitted photons without and with dissipation, respectively.

#### 5. Single-photon entanglement generation

In this paper, we show that a spontaneously emitted photon from a locally coupled quantum emitter will be distributed over multiple boundary modes, and we point out that this will lead to a single-particle entangled states between the different channels [65]. In this section, we give the analytical expression of such photonic state within the Markovian approximation, and we quantify its entanglement. Let us first determine the asymptotic photonic state. After a time  $t \gg \Gamma^{-1}$ , the emitter population will be negligible and the state will be purely photonic, i.e.,  $e^{-iHt}|e\rangle \otimes |\text{vac}\rangle \approx |g\rangle \otimes |\Psi_{\text{ph}}\rangle$ . Assuming a multimode waveguide of boundary modes and letting  $A_{l,\mathbf{k}}$  be the annihilation operator for a photon in the  $l$ th

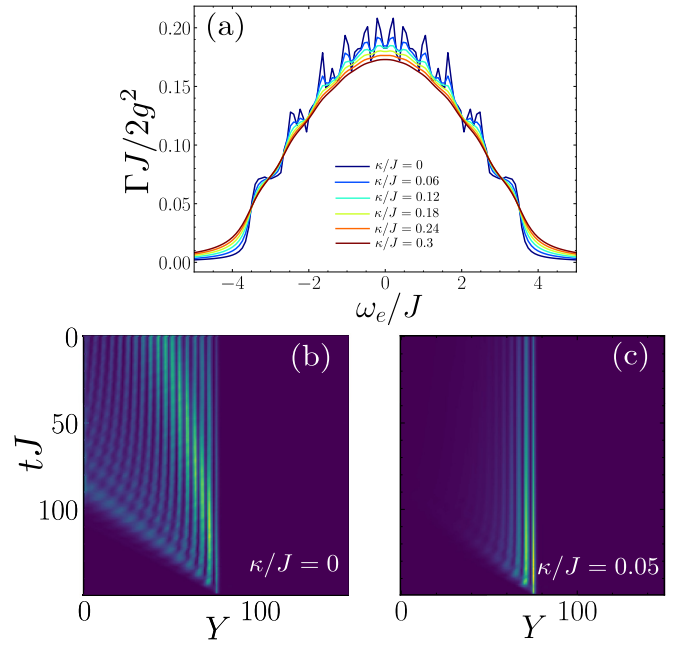


FIG. 14. (a) Markovian decay rate of a quantum emitter coupled at the edge of a HH lattice of  $40 \times 40$  and  $\phi = 1/12$ , for several values of the local mode loss rate  $\kappa$ . (b), (c) Excitation dynamics along the left boundary of a HH lattice with flux  $\phi = 1/12$ , induced by the spontaneous emission of a quantum emitter with energy  $\omega_e/J = -2.48$ , resonant to two edge modes, and a local loss rate of (a)  $\kappa/J = 0$  and (b)  $\kappa/J = 0.05$  on the lattice sites. We observe two light cones, associated with the two group velocities of both topological channels.

mode with quasimomentum  $\mathbf{k}$ , we can rewrite the light-matter Hamiltonian as

$$\begin{aligned} H = & \omega_e \sigma_{ee} + \sum_l \sum_{\mathbf{k}} \omega_l(\mathbf{k}) A_{l,\mathbf{k}}^{\dagger} A_{l,\mathbf{k}} + \sigma_{eg} \left( \sum_l \sum_{\mathbf{k}} g_{l,\mathbf{k}} A_{l,\mathbf{k}} \right) \\ & + \text{H.c.} \end{aligned} \quad (\text{C17})$$

with  $g_{l,\mathbf{k}} = \sqrt{\Gamma_l/(2\pi)}$ , where  $\Gamma_l$  is the expected Markovian decay rate in the  $\Gamma_l$  mode. Since the Hamiltonian preserves the number of excitations, if the emitter is initially excited, one can write the quantum state of the emitter+ bath system at any time as follows:  $|\Psi(t)\rangle = C_e(t)|e\rangle \otimes |\text{vac}\rangle + \sum_{\mathbf{k}} C_{\mathbf{k}}(t)|g\rangle \otimes a_{\mathbf{k}}^{\dagger}|\text{vac}\rangle$ . Applying the time-dependent Schrödinger equation to this wave function, one can obtain the following set of equations for the time-dependent coefficients:

$$\begin{aligned} \frac{\partial C_e(t)}{\partial t} = & \sum_l \sum_{\mathbf{k}} i g_{l,\mathbf{k}} e^{i[\omega_e - \omega_l(\mathbf{k})]t} C_{\mathbf{k}}(t), \\ \frac{\partial C_{\mathbf{k}}(t)}{\partial t} = & \sum_l i g_{l,\mathbf{k}}^* e^{i[\omega_l(\mathbf{k}) - \omega_e]t} C_e(t). \end{aligned} \quad (\text{C18})$$

Formally integrating the second equation, inserting in the first equation, and applying Markov approximation, we find that the emitter follows exponential decay  $C_e(t) \approx e^{-\Gamma t/2}$ , where

$\Gamma = \sum_l \Gamma_l$ . Then

$$\begin{aligned} C_{\mathbf{k}}(t) &\approx \sum_l \int_0^t d\tau i g_{l,\mathbf{k}} e^{i[\omega_l(\mathbf{k}) - \omega_e]\tau} e^{-\Gamma\tau/2} \\ &\approx \sum_l \sqrt{\frac{\Gamma_l}{2\pi}} \frac{e^{i[\omega_l(\mathbf{k}) - \omega_e]t}}{\omega_l(\mathbf{k}) - \omega_e + i\Gamma/2}, \end{aligned} \quad (\text{C19})$$

where we assumed  $t \gg \Gamma^{-1}$ . We conclude that the asymptotic photonic state  $|\Psi_{\text{ph}}\rangle$  can be written as

$$|\Psi_{\text{ph}}\rangle = \sum_{l,\mathbf{k}} \sqrt{\frac{\Gamma_l}{2\pi}} \frac{e^{-i\omega_l(\mathbf{k})t}}{\omega_l(\mathbf{k}) - \omega_e + i\Gamma/2} |n_l \mathbf{k}\rangle. \quad (\text{C20})$$

For a single mode, we recover the well-known expression for the asymptotic photonic state of the emitted light from an emitter coupled to a single-mode waveguide [107]. From this expression, we observe that the contribution of the  $l$ th mode to the asymptotic photonic state population is weighted by  $\sqrt{\Gamma_l}$ . Defining a multimode basis  $\{|1_l\rangle\}$ , where  $|1_l\rangle$  contains one photon in the  $l$ th mode, and defining  $C_l = \sqrt{\Gamma_l/\Gamma}$  we can write the photonic state whose entanglement we want to characterize as

$$|\Psi_{\text{ph}}\rangle = \sum_l C_l |1_l\rangle. \quad (\text{C21})$$

Here, we are consciously neglecting the contribution of the different phases between the modes, since in principle they can be corrected by local operations, and thus should not contribute to the entanglement measures. One way of characterizing the entanglement of this class of states is by calculating the entanglement entropy [66] between the different topological channels. The entanglement entropy of a given state  $\Psi$  for a bipartition of the Hilbert space  $\mathbb{H}_A \otimes \mathbb{H}_B$  reads [66]

$$E(|\Psi\rangle\langle\Psi|) \equiv S(\text{Tr}_A |\Psi\rangle\langle\Psi|) = S(\text{Tr}_B |\Psi\rangle\langle\Psi|), \quad (\text{C22})$$

where  $S(\rho) = -\text{Tr}(\rho \ln \rho)$  and  $\text{Tr}_{A/B}$  denotes the partial trace along the  $A/B$  subspace. In our case, we define as  $P_l$  to the bipartition separating the  $l$ th mode from the rest. Assuming a bipartition  $P_l$ , we will take our Hilbert space as  $\mathbb{H}_l \oplus (\oplus_{l' \neq l} \mathbb{H}_{l'})$ , and denote by  $|10\rangle$  ( $|01\rangle$ ) the state with one excitation in the  $l$ th mode and zero in the rest (and vice versa). From Eq. (C21), and using that notation, we then know we can always write our state as

$$|\psi_{\text{ph}}\rangle = C_l |10\rangle + \sqrt{1 - |C_l|^2} |01\rangle. \quad (\text{C23})$$

Denoting by  $p = |C_l|^2$  the probability of measuring the photon in the  $l$ th mode, the entanglement entropy of this state can be readily computed as

$$E(|\psi_{\text{ph}}\rangle\langle\psi_{\text{ph}}|) = -p \log p - (1-p) \log(1-p). \quad (\text{C24})$$

In Fig. 15, we present the entanglement entropy for all possible bipartitions in each spectral band gap, in comparison with the entanglement entropy of a  $W$  state with a number of qubits equal to the number of resonant edge modes in each band gap (dashed lines). The latter can be calculated by imposing  $p = 1/N_{\text{modes}}$  in Eq. (C24). In the figure, we observe that the entanglement of our generated state is very similar to the one obtained for a maximally entangled  $W$  state in all the band

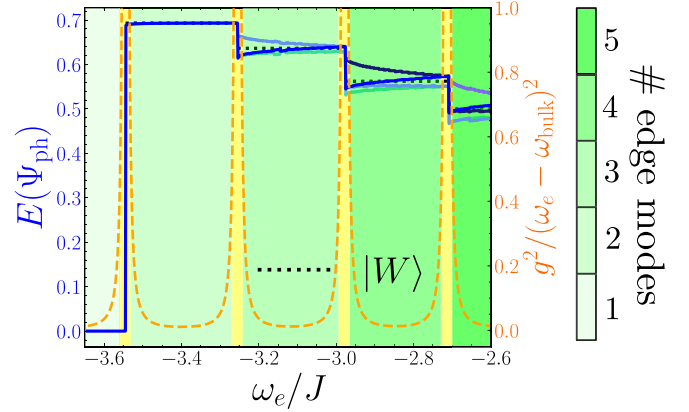


FIG. 15. Quantifying single-particle entanglement of spontaneously emitted photon states. For a Harper-Hofstadter lattice of  $\phi = 1/25$ , we represent the entanglement entropy for all possible bipartitions (blue solid lines) and the approximate population of the bulk modes obtained using a perturbative approximation (orange dashed line) for different values of the emitter transition frequency. Yellow regions depict the location of the Landau levels. Horizontal black dotted lines represent the entanglement entropy benchmark for  $W$  states with a number of qubits equal to the number of resonant edge modes in each band gap.

gaps. Let us note that this calculation is done assuming that the emitter only decays through the edge modes. This will be a good approximation as long as the population of the bulk modes remains small. The latter can be perturbatively approximated by  $g^2/(\omega_e - \omega_{\text{bulk}})^2$ , which is what we plot in dashed orange curves in Fig. 15. Thus, the calculation of the entanglement entropy will be valid outside of the yellow regions where the population into the Landau levels become negligible. To make a more quantitative estimation of the impact of the bulk modes on the generated entanglement, one can use more sophisticated entanglement measures, such as the negativity [108], that can be effectively computed for mixed states. However, we believe that for the sake of illustration the entanglement entropy between the different channels represents a more intuitive witness.

## 6. Mode selectivity using nonlocal couplings

Local light-matter Hamiltonians, such as the ones considered in Eq. (C1), lead to completely delocalized couplings in momentum space. For example, assuming the cylinder geometry that we considered in the previous section, one can rewrite the light-matter Hamiltonian  $H_l$  as follows:

$$H_l = g \sigma_{eg} a_{\mathbf{r}_e} + \text{H.c.} = \sum_{k_y} \left( \frac{g}{\sqrt{L_y}} \sigma_{eg} a_{(x_e, k_y)} e^{-ik_y y_e} + \text{H.c.} \right), \quad (\text{C25})$$

where

$$a_{(x_e, k_y)} = \frac{1}{\sqrt{L_y}} \sum_y a_{(x_e, y)} e^{-ik_y y}. \quad (\text{C26})$$

As a result, when coupling an emitter with an optical transition of a given energy  $\omega_e$ , it couples to all the edge modes of a given energy. Thus, a quantum emitter locally coupled to the

edge of a HH lattice will couple to all topological channels. In this section, we address the problem of selecting the channels to which the quantum emitter can decay by using nonlocal couplings such that the emitted photon couples selectively to some of the topological channels. The key point is that if one lets the emitter couple to several edge sites with different strengths  $g_j$ , the light-matter coupling acquires a  $\mathbf{k}$  dependence depending on these couplings:

$$H_I = \sum_y g_y \sigma_{eg} a_{(x,y)} + \text{H.c.} = \sum_{k_y} [G(k_y) \sigma_{eg} a_{(x_e, k_y)} + \text{H.c.}], \quad (\text{C27})$$

with

$$G(k_y) = \frac{1}{\sqrt{L_y}} \sum_y g_y e^{-ik_y y}. \quad (\text{C28})$$

Such  $\mathbf{k}$ -dependent coupling can be used to cancel the coupling to certain momenta and thus prevent the emission in these modes. For example, this has been used in one- [84] and two-dimensional [54] single-mode waveguides to generate chiral, one-directional emission in baths with isotropic bath dispersions. In our topological multimode wave guides, for fixed  $\omega_e$ , the resonant modes feature a different resonant  $k_e^{(l)}$ . Thus, choosing  $g_y$  such that  $G(k_e^{(l)}) = 0$  to some of the modes, one can selectively couple to the other ones. Let us now illustrate a potential method to achieve that selectivity inspired by the results in Refs. [54,84] that one only requires coupling to  $N_c + 1$  cavities if one wants to cancel the coupling to  $N_c$  resonant momenta  $k_e^{(l)}$ . Let us start with the case where we want cancel only the coupling to a single resonant momentum  $k_e^{(l)}$ . For that, let us assume that the emitter couples to neighboring sites with the same amplitude, but a relative complex phase  $\varphi_l$ , that is,  $g_y = g$ ,  $g_{y+1} = g e^{i\varphi_l}$ . Using these values, it can be shown from Eq. (C28) that

$$|G_{\varphi_l}(k_y)|^2 = \frac{2g^2}{L_y} [1 + \cos(k_y + \varphi_l)]. \quad (\text{C29})$$

Thus, if we want to make it zero for certain  $k_y = k_e^{(l)}$ , we just have to choose a relative phase:  $\varphi_{l,e} = \pi - k_e^{(l)}$ . In the case

where there are more than two edge modes, one might be interested in canceling the coupling to two or more momenta. A way of doing that would be to obtain an effective  $G(k_y)$  out of the product required to cancel each momentum, separately. In the general case, where we are interested in suppressing  $N_k$  modes, such a proposal implies taking  $G(k_y)$  as

$$G(k_y) = \prod_{\delta=0}^{N_k-1} G_{\varphi_\delta}(k_y), \quad (\text{C30})$$

where  $\varphi_\delta = \pi - k_e^{(\delta)}$ . With this choice, we get a nonlocal coupling in  $\mathbf{k}$  space of the form

$$\begin{aligned} G(k_y) &= \prod_{\delta=0}^{N_k-1} (1 + e^{i(\varphi_\delta - k_y)}) \\ &= \sum_{M=0}^{N_k-1} e^{-iMk_y} \sum_{|\Omega|=M} \exp\left(i \sum_{\delta \in \Omega} \varphi_\delta\right), \end{aligned} \quad (\text{C31})$$

where the sum over  $|\Omega| = M$  denotes a sum over all the  $N_k!/M!(N_k - M)!$  subsets of  $\{1, 2, \dots, N_k\}$  with  $M$  elements. From this expansion in powers of  $e^{-ik_y}$ , we can directly read the couplings in real space

$$g_{(0,y+M)} = \sum_{|\Omega|=M} \exp\left(i \sum_{\delta \in \Omega} \varphi_\delta\right), \quad (\text{C32})$$

with  $M = 0, \dots, N_k - 1$ . This shows that the number of nonlocal couplings required to cancel  $N_k$  modes scales linearly with  $N_k$ , although this method will be eventually limited by the capacity to resolve the modes. As an example, for  $N_k = 2$  we have

$$G_{\varphi_0, \varphi_1}(k_y) \propto 1 + (e^{i\varphi_0} + e^{i\varphi_1})e^{ik_y} + e^{i(\varphi_0 + \varphi_1)}e^{i2k_y}, \quad (\text{C33})$$

which can be achieved with real-space couplings of the form  $g_{(0,y)} = g$ ,  $g_{(0,y+1)} = g e^{i\varphi_0} + g e^{i\varphi_1}$  and  $g_{(0,y+2)} = g e^{i(\varphi_0 + \varphi_1)}$ .

- 
- [1] T. Ozawa, H. M. Price, A. Amo, N. Goldman, M. Hafezi, L. Lu, M. C. Rechtsman, D. Schuster, J. Simon, O. Zilberberg, and I. Carusotto, Topological photonics, *Rev. Mod. Phys.* **91**, 015006 (2019).
- [2] M. S. Rider, S. J. Palmer, S. R. Pockock, X. Xiao, P. Arroyo Huidobro, and V. Giannini, A perspective on topological nanophotonics: Current status and future challenges, *J. Appl. Phys.* **125**, 120901 (2019).
- [3] D. Smirnova, D. Leykam, Y. Chong, and Y. Kivshar, Nonlinear topological photonics, *Appl. Phys. Rev.* **7**, 021306 (2020).
- [4] H. Price, Y. Chong, A. Khanikaev, H. Schomerus, L. J. Maczewsky, M. Kremer, M. Heinrich, A. Szameit, O. Zilberberg, Y. Yang, B. Zhang, A. Alù, R. Thomale, I. Carusotto, P. St-Jean, A. Amo, A. Dutt, L. Yuan, S. Fan, X. Yin, C. Peng, T. Ozawa, and A. Blanco-Redondo, Roadmap on topological photonics, *J. Phys. Photonics* **4**, 032501 (2022).
- [5] F. D. M. Haldane and S. Raghu, Possible Realization of Directional Optical Waveguides in Photonic Crystals with Broken Time-Reversal Symmetry, *Phys. Rev. Lett.* **100**, 013904 (2008).
- [6] S. Raghu, X. L. Qi, C. Honerkamp, and S. C. Zhang, Topological Mott Insulators, *Phys. Rev. Lett.* **100**, 156401 (2008).
- [7] Z. Wang, Y. Chong, J. D. Joannopoulos, and M. Soljačić, Observation of unidirectional backscattering-immune topological electromagnetic states, *Nature (London)* **461**, 772 (2009).
- [8] M. C. Rechtsman, Y. Plotnik, J. M. Zeuner, D. Song, Z. Chen, A. Szameit, and M. Segev, Topological Creation and Destruction of Edge States in Photonic Graphene, *Phys. Rev. Lett.* **111**, 103901 (2013).
- [9] M. Hafezi, S. Mittal, J. Fan, A. Migdall, and J. M. Taylor, Imaging topological edge states in silicon photonics, *Nat. Photonics* **7**, 1001 (2013).



- [10] B. Bahari, A. Ndao, F. Vallini, A. El Amili, Y. Fainman, and B. Kanté, Nonreciprocal lasing in topological cavities of arbitrary geometries, *Science* **358**, 636 (2017).
- [11] M. A. Bandres, S. Wittek, G. Harari, M. Parto, J. Ren, M. Segev, D. N. Christodoulides, and M. Khajavikhan, Topological insulator laser: Experiments, *Science* **359**, eaar4005 (2018).
- [12] S. Klemmt, T. H. Harder, O. A. Egorov, K. Winkler, R. Ge, M. A. Bandres, M. Emmerling, L. Worschech, T. C. Liew, M. Segev, C. Schneider, and S. Höfling, Exciton-polariton topological insulator, *Nature (London)* **562**, 552 (2018).
- [13] I. Amelio and I. Carusotto, Theory of the Coherence of Topological Lasers, *Phys. Rev. X* **10**, 041060 (2020).
- [14] S. Barik, A. Karasahin, C. Flower, T. Cai, H. Miyake, W. DeGottardi, M. Hafezi, and E. Waks, A topological quantum optics interface, *Science* **359**, 666 (2018).
- [15] S. Barik, A. Karasahin, S. Mittal, E. Waks, and M. Hafezi, Chiral quantum optics using a topological resonator, *Phys. Rev. B* **101**, 205303 (2020).
- [16] D. Hallett, A. P. Foster, D. Whittaker, M. S. Skolnick, and L. R. Wilson, Engineering chiral light-matter interactions in a waveguide-coupled nanocavity, *ACS Photonics* **9**, 706 (2022).
- [17] M. J. Mehrabad, A. P. Foster, R. Dost, E. Clarke, P. K. Patil, A. M. Fox, M. S. Skolnick, and L. R. Wilson, Chiral topological photonics with an embedded quantum emitter, *Optica* **7**, 1690 (2020).
- [18] J. C. Owens, M. G. Panetta, B. Saxberg, G. Roberts, S. Chakram, R. Ma, A. Vrajitoarea, J. Simon, and D. Schuster, Chiral cavity quantum electrodynamics, *Nat. Phys.* **18**, 1048 (2022).
- [19] S. Mittal, V. V. Orre, and M. Hafezi, Topologically robust transport of entangled photons in a 2D photonic system, *Opt. Express* **24**, 15631 (2016).
- [20] S. Mittal, E. A. Goldschmidt, and M. Hafezi, A topological source of quantum light, *Nature (London)* **561**, 502 (2018).
- [21] S. Mittal, V. V. Orre, E. A. Goldschmidt, and M. Hafezi, Tunable quantum interference using a topological source of indistinguishable photon pairs, *Nat. Photonics* **15**, 542 (2021).
- [22] A. Blanco-Redondo, B. Bell, D. Oren, B. J. Eggleton, and M. Segev, Topological protection of biphoton states, *Science* **362**, 568 (2018).
- [23] M. Wang, C. Doyle, B. Bell, M. J. Collins, E. Magi, B. J. Eggleton, M. Segev, and A. Blanco-Redondo, Topologically protected entangled photonic states, *Nanophotonics* **8**, 1327 (2019).
- [24] A. Blanco-Redondo, Topological nanophotonics: Toward robust quantum circuits, *Proc. IEEE* **108**, 837 (2020).
- [25] C. Doyle, W.-W. Zhang, M. Wang, B. A. Bell, S. D. Bartlett, and A. Blanco-Redondo, Biphoton entanglement of topologically distinct modes, *Phys. Rev. A* **105**, 023513 (2022).
- [26] N. Y. Yao, C. R. Laumann, A. V. Gorshkov, H. Weimer, L. Jiang, J. I. Cirac, P. Zoller, and M. D. Lukin, Topologically protected quantum state transfer in a chiral spin liquid, *Nat. Commun.* **4**, 1585 (2013).
- [27] M. A. Lemonde, V. Peano, P. Rabl, and D. G. Angelakis, Quantum state transfer via acoustic edge states in a 2D optomechanical array, *New J. Phys.* **21**, 113030 (2019).
- [28] J. Cao, W. X. Cui, X. Yi, and H. F. Wang, Topological phase transition and topological quantum state transfer in periodically modulated circuit-QED lattice, *Ann. Phys. (Berlin)* **533**, 2100120 (2021).
- [29] C. Dłaska, B. Vermersch, and P. Zoller, Robust quantum state transfer via topologically protected edge channels in dipolar arrays, *Quantum Sci. Technol.* **2**, 015001 (2017).
- [30] G. M. A. Almeida, F. Ciccarello, T. J. G. Apollaro, and A. M. C. Souza, Quantum-state transfer in staggered coupled-cavity arrays, *Phys. Rev. A* **93**, 032310 (2016).
- [31] F. Mei, G. Chen, L. Tian, S. L. Zhu, and S. Jia, Robust quantum state transfer via topological edge states in superconducting qubit chains, *Phys. Rev. A* **98**, 012331 (2018).
- [32] N. Lang and H. P. Büchler, Topological networks for quantum communication between distant qubits, *npj Quantum Inf.* **3**, 47 (2017).
- [33] S. Longhi, G. L. Giorgi, and R. Zambrini, Landau-Zener topological quantum state transfer, *Adv. Quantum Technol.* **2**, 1800090 (2019).
- [34] M. C. Tran, A. Deshpande, A. Y. Guo, A. Lucas, and A. V. Gorshkov, Optimal State Transfer and Entanglement Generation in Power-Law Interacting Systems, *Phys. Rev. X* **11**, 031016 (2021).
- [35] C. Wang, L. Li, J. Gong, and Y.-x. Liu, Arbitrary entangled state transfer via a topological qubit chain, *Phys. Rev. A* **106**, 052411 (2022).
- [36] J. X. Han, J. L. Wu, Y. Wang, Y. Xia, Y. Y. Jiang, and J. Song, Large-scale Greenberger-Horne-Zeilinger states through a topologically protected zero-energy mode in a superconducting qutrit-resonator chain, *Phys. Rev. A* **103**, 032402 (2021).
- [37] S. A. Skirlo, L. Lu, and M. Soljačić, Multimode One-Way Waveguides of Large Chern Numbers, *Phys. Rev. Lett.* **113**, 113904 (2014).
- [38] S. A. Skirlo, L. Lu, Y. Igarashi, Q. Yan, J. Joannopoulos, and M. Soljačić, Experimental Observation of Large Chern Numbers in Photonic Crystals, *Phys. Rev. Lett.* **115**, 253901 (2015).
- [39] M. Bello, G. Platero, J. I. Cirac, and A. González-Tudela, Unconventional quantum optics in topological waveguide QED, *Sci. Adv.* **5**, eaaw0297 (2019).
- [40] L. Leonforte, A. Carollo, and F. Ciccarello, Vacancy-like Dressed States in Topological Waveguide QED, *Phys. Rev. Lett.* **126**, 063601 (2021).
- [41] C. Vega, M. Bello, D. Porrás, and A. González-Tudela, Qubit-photon bound states in topological waveguides with long-range hoppings, *Phys. Rev. A* **104**, 053522 (2021).
- [42] D. De Bernardis, Z.-P. Cian, I. Carusotto, M. Hafezi, and P. Rabl, Light-Matter Interactions in Synthetic Magnetic Fields: Landau-Photon Polaritons, *Phys. Rev. Lett.* **126**, 103603 (2021).
- [43] I. García-Elcano, A. González-Tudela, and J. Bravo-Abad, Tunable and Robust Long-Range Coherent Interactions between Quantum Emitters Mediated by Weyl Bound States, *Phys. Rev. Lett.* **125**, 163602 (2020).
- [44] I. n. García-Elcano, J. Bravo-Abad, and A. González-Tudela, Light-matter interactions near photonic Weyl points, *Phys. Rev. A* **103**, 033511 (2021).
- [45] M. Bello, G. Platero, and A. González-Tudela, Spin many-body phases in standard- and topological-waveguide QED simulators, *PRX Quantum* **3**, 010336 (2022).

- [46] F. Grusdt, M. Hönig, and M. Fleischhauer, Topological Edge States in the One-Dimensional Superlattice Bose-Hubbard Model, *Phys. Rev. Lett.* **110**, 260405 (2013).
- [47] F. Grusdt, F. Letscher, M. Hafezi, and M. Fleischhauer, Topological Growing of Laughlin States in Synthetic Gauge Fields, *Phys. Rev. Lett.* **113**, 155301 (2014).
- [48] M. F. Maghrebi, N. Y. Yao, M. Hafezi, T. Pohl, O. Firstenberg, and A. V. Gorshkov, Fractional quantum Hall states of Rydberg polaritons, *Phys. Rev. A* **91**, 033838 (2015).
- [49] N. Schine, A. Ryou, A. Gromov, A. Sommer, and J. Simon, Synthetic Landau levels for photons, *Nature (London)* **534**, 671 (2016).
- [50] L. W. Clark, N. Schine, C. Baum, N. Jia, and J. Simon, Observation of Laughlin states made of light, *Nature (London)* **582**, 41 (2020).
- [51] E. Kim, X. Zhang, V. S. Ferreira, J. Banker, J. K. Iverson, A. Sipahigil, M. Bello, A. González-Tudela, M. Mirhosseini, and O. Painter, Quantum Electrodynamics in a Topological Waveguide, *Phys. Rev. X* **11**, 011015 (2021).
- [52] S. C. Wein, J. C. Loredó, M. Maffei, P. Hilaire, A. Harouri, N. Somaschi, A. Lemaître, I. Sagnes, L. Lanco, O. Krebs, A. Auffèves, C. Simon, P. Senellart, and C. Antón-Solanas, Photon-number entanglement generated by sequential excitation of a two-level atom, *Nat. Photonics* **16**, 374 (2022).
- [53] A. F. Kockum, G. Johansson, and F. Nori, Decoherence-Free Interaction between Giant Atoms in Waveguide Quantum Electrodynamics, *Phys. Rev. Lett.* **120**, 140404 (2018).
- [54] A. González-Tudela, C. S. Muñoz, and J. I. Cirac, Engineering and Harnessing Giant Atoms in High-Dimensional Baths: A Proposal for Implementation with Cold Atoms, *Phys. Rev. Lett.* **122**, 203603 (2019).
- [55] A. Frisk Kockum, *Quantum Optics with Giant Atoms—the First Five Years* (Springer, Singapore, 2021), pp. 125–146.
- [56] B. Kannan, M. J. Ruckriegel, D. L. Campbell, A. Frisk Kockum, J. Braumüller, D. K. Kim, M. Kjaergaard, P. Krantz, A. Melville, B. M. Niedzielski, A. Vepsäläinen, R. Winik, J. L. Yoder, F. Nori, T. P. Orlando, S. Gustavsson, and W. D. Oliver, Waveguide quantum electrodynamics with superconducting artificial giant atoms, *Nature (London)* **583**, 775 (2020).
- [57] X. Wang, T. Liu, A. F. Kockum, H. R. Li, and F. Nori, Tunable Chiral Bound States with Giant Atoms, *Phys. Rev. Lett.* **126**, 043602 (2021).
- [58] G. L. Giorgi, S. Longhi, A. Cabot, and R. Zambrini, Quantum probing topological phase transitions by non-markovianity, *Ann. Phys. (Berlin)* **531**, 1900307 (2019).
- [59] D. R. Hofstadter, Energy levels and wave functions of Bloch electrons in rational and irrational magnetic fields, *Phys. Rev. B* **14**, 2239 (1976).
- [60] F. Harper, S. H. Simon, and R. Roy, Perturbative approach to flat Chern bands in the Hofstadter model, *Phys. Rev. B* **90**, 075104 (2014).
- [61] N. Goldman, Characterizing the Hofstadter butterfly’s outline with Chern numbers, *J. Phys. B: At., Mol. Opt. Phys.* **42**, 055302 (2009).
- [62] As shown in the Appendixes, this situation is qualitatively equivalent to the case where the multiple edge states emerge from a single band with  $|C| > 1$  [37,38].
- [63] C. Cohen-Tannoudji, J. Dupont-Roc, and G. Grynberg, *Atom-Photon Interactions: Basic Processes and Applications* (Wiley-VCH, Weinheim, 2004).
- [64] C. K. Law and H. J. Kimble, Deterministic generation of a bit-stream of single-photon pulses, *J. Mod. Opt.* **44**, 2067 (1997).
- [65] S. J. van Enk, Single-particle entanglement, *Phys. Rev. A* **72**, 064306 (2005).
- [66] C. H. Bennett, G. Brassard, S. Popescu, B. Schumacher, J. A. Smolin, and W. K. Wootters, Purification of Noisy Entanglement and Faithful Teleportation via Noisy Channels, *Phys. Rev. Lett.* **76**, 722 (1996).
- [67] W. Dur, G. Vidal, and J. I. Cirac, Three qubits can be entangled in two inequivalent ways, *Phys. Rev. A* **62**, 062314 (2000).
- [68] K. M. Gheri, C. Saavedra, P. Törmä, J. I. Cirac, and P. Zoller, Entanglement engineering of one-photon wave packets using a single-atom source, *Phys. Rev. A* **58**, R2627 (1998).
- [69] C. Saavedra, K. M. Gheri, P. Törmä, J. I. Cirac, and P. Zoller, Controlled source of entangled photonic qubits, *Phys. Rev. A* **61**, 062311 (2000).
- [70] C. Schön, E. Solano, F. Verstraete, J. I. Cirac, and M. M. Wolf, Sequential Generation of Entangled Multiqubit States, *Phys. Rev. Lett.* **95**, 110503 (2005).
- [71] N. H. Lindner and T. Rudolph, Proposal for Pulsed On-Demand Sources of Photonic Cluster State Strings, *Phys. Rev. Lett.* **103**, 113602 (2009).
- [72] S. E. Economou, N. Lindner, and T. Rudolph, Optically Generated 2-Dimensional Photonic Cluster State from Coupled Quantum Dots, *Phys. Rev. Lett.* **105**, 093601 (2010).
- [73] I. Schwartz, D. Cogan, E. R. Schmidgall, Y. Don, L. Gantz, O. Kenneth, N. H. Lindner, and D. Gershoni, Deterministic generation of a cluster state of entangled photons, *Science* **354**, 434 (2016).
- [74] H. Pichler, S. Choi, P. Zoller, and M. D. Lukin, Universal photonic quantum computation via time-delayed feedback, *Proc. Natl. Acad. Sci. USA* **114**, 11362 (2017).
- [75] J. Borregaard, H. Pichler, T. Schröder, M. D. Lukin, P. Lodahl, and A. S. Sørensen, One-Way Quantum Repeater Based on Near-Deterministic Photon-Emitter Interfaces, *Phys. Rev. X* **10**, 021071 (2020).
- [76] K. Tiurev, M. H. Appel, P. L. Mirambell, M. B. Lauritzen, A. Tiranov, P. Lodahl, and A. S. Sørensen, High-fidelity multiphoton-entangled cluster state with solid-state quantum emitters in photonic nanostructures, *Phys. Rev. A* **105**, L030601 (2022).
- [77] M. Gimeno-Segovia, T. Rudolph, and S. E. Economou, Deterministic Generation of Large-Scale Entangled Photonic Cluster State from Interacting Solid State Emitters, *Phys. Rev. Lett.* **123**, 070501 (2019).
- [78] P. Kurpiers, M. Pechal, B. Royer, P. Magnard, T. Walter, J. Heinsoo, Y. Salathé, A. Akin, S. Storz, J. C. Besse, S. Gasparinetti, A. Blais, and A. Wallraff, Quantum Communication with Time-Bin Encoded Microwave Photons, *Phys. Rev. Appl.* **12**, 044067 (2019).
- [79] J. C. Besse, K. Reuer, M. C. Collodo, A. Wulff, L. Wernli, A. Copetudo, D. Malz, P. Magnard, A. Akin, M. Gabureac, G. J. Norris, J. I. Cirac, A. Wallraff, and C. Eichler, Realizing a deterministic source of multipartite-entangled photonic qubits, *Nat. Commun.* **11**, 4877 (2020).
- [80] B. Kannan, D. L. Campbell, F. Vasconcelos, R. Winik, D. K. Kim, M. Kjaergaard, P. Krantz, A. Melville, B. M. Niedzielski,

- J. L. Yoder, T. P. Orlando, S. Gustavsson, and W. D. Oliver, Generating spatially entangled itinerant photons with waveguide quantum electrodynamics, *Sci. Adv.* **6**, eabb8780 (2020).
- [81] Z. Y. Wei, D. Malz, A. González-Tudela, and J. I. Cirac, Generation of photonic matrix product states with Rydberg atomic arrays, *Phys. Rev. Res.* **3**, 023021 (2021).
- [82] Z. Y. Wei, D. Malz, and J. I. Cirac, Sequential Generation of Projected Entangled-Pair States, *Phys. Rev. Lett.* **128**, 010607 (2022).
- [83] V. S. Ferreira, G. Kim, A. Butler, H. Pichler, and O. Painter, Deterministic generation of multidimensional photonic cluster states with a single quantum emitter, [arXiv:2206.10076](https://arxiv.org/abs/2206.10076).
- [84] T. Ramos, B. Vermersch, P. Hauke, H. Pichler, and P. Zoller, Non-Markovian dynamics in chiral quantum networks with spins and photons, *Phys. Rev. A* **93**, 062104 (2016).
- [85] P. O. Guimond, B. Vermersch, M. L. Juan, A. Sharafiev, G. Kirchmair, and P. Zoller, A unidirectional on-chip photonic interface for superconducting circuits, *npj Quantum Inf.* **6**, 32 (2020).
- [86] A. Soro and A. F. Kockum, Chiral quantum optics with giant atoms, *Phys. Rev. A* **105**, 023712 (2022).
- [87] P. Lodahl, S. Mahmoodian, S. Stobbe, A. Rauschenbeutel, P. Schneeweiss, J. Volz, H. Pichler, and P. Zoller, Chiral quantum optics, *Nature (London)* **541**, 473 (2017).
- [88] B. Schriniski, M. Lamaison, and A. S. Sørensen, Passive Quantum Phase Gate for Photons Based on Three Level Emitters, *Phys. Rev. Lett.* **129**, 130502 (2022).
- [89] M. C. Rechtsman, Y. Lumer, Y. Plotnik, A. Perez-Leija, A. Szameit, and M. Segev, Topological protection of photonic path entanglement, *Optica* **3**, 925 (2016).
- [90] T. Dai, Y. Ao, J. Bao, J. Mao, Y. Chi, Z. Fu, Y. You, X. Chen, C. Zhai, B. Tang, Y. Yang, Z. Li, L. Yuan, F. Gao, X. Lin, M. G. Thompson, J. L. O'Brien, Y. Li, X. Hu, Q. Gong, and J. Wang, Topologically protected quantum entanglement emitters, *Nat. Photonics* **16**, 248 (2022).
- [91] K. Tschernig, I. Jimenez-Galán, D. N. Christodoulides, M. Ivanov, K. Busch, M. A. Bandres, and A. Perez-Leija, Topological protection versus degree of entanglement of two-photon light in photonic topological insulators, *Nat. Commun.* **12**, 1974 (2021).
- [92] D. Porras and S. Fernández-Lorenzo, Topological Amplification in Photonic Lattices, *Phys. Rev. Lett.* **122**, 143901 (2019).
- [93] C. C. Wanjura, M. Brunelli, and A. Nunnenkamp, Topological framework for directional amplification in driven-dissipative cavity arrays, *Nat. Commun.* **11**, 3149 (2020).
- [94] T. Ramos, J. J. Garcia-Ripoll, and D. Porras, Topological input-output theory for directional amplification, *Phys. Rev. A* **103**, 033513 (2021).
- [95] A. Gómez-León, T. Ramos, A. González-Tudela, and D. Porras, Bridging the gap between topological non-Hermitian physics and open quantum systems, *Phys. Rev. A* **106**, L011501 (2022).
- [96] Z. Gong, Y. Ashida, K. Kawabata, K. Takasan, S. Higashikawa, and M. Ueda, Topological Phases of Non-Hermitian Systems, *Phys. Rev. X* **8**, 031079 (2018).
- [97] K. Kawabata, K. Shiozaki, M. Ueda, and M. Sato, Symmetry and Topology in Non-Hermitian Physics, *Phys. Rev. X* **9**, 041015 (2019).
- [98] H. G. Zirnstein and B. Rosenow, Exponentially growing bulk Green functions as signature of nontrivial non-Hermitian winding number in one dimension, *Phys. Rev. B* **103**, 195157 (2021).
- [99] A. McDonald, T. Pereg-Barnea, and A. A. Clerk, Phase-Dependent Chiral Transport and Effective Non-Hermitian Dynamics in a Bosonic Kitaev-Majorana Chain, *Phys. Rev. X* **8**, 041031 (2018).
- [100] A. McDonald and A. A. Clerk, Exponentially-enhanced quantum sensing with non-Hermitian lattice dynamics, *Nat. Commun.* **11**, 5382 (2020).
- [101] A. McDonald, R. Hanai, and A. A. Clerk, Non-equilibrium stationary states of quantum non-Hermitian lattice models, *Phys. Rev. B* **105**, 064302 (2022).
- [102] M. Trescher and E. J. Bergholtz, Flat bands with higher Chern number in pyrochlore slabs, *Phys. Rev. B* **86**, 241111(R) (2012).
- [103] M. Udagawa and E. J. Bergholtz, Correlations and entanglement in flat band models with variable Chern numbers, *J. Stat. Mech.: Theory Exp.* (2014) P10012.
- [104] E. J. Bergholtz, Z. Liu, M. Trescher, R. Moessner, and M. Udagawa, Topology and Interactions in a Frustrated Slab: Tuning from Weyl Semimetals to  $C > 1$  Fractional Chern Insulators, *Phys. Rev. Lett.* **114**, 016806 (2015).
- [105] H. Zhang, J. Li, H. Jiang, N. Li, J. Wang, J. Xu, C. Zhu, and Y. Yang, Coherent interaction of a quantum emitter and the edge states in two-dimensional optical topological insulators, *Phys. Rev. A* **105**, 053703 (2022).
- [106] E. Fermi, Quantum theory of radiation, *Rev. Mod. Phys.* **4**, 87 (1932).
- [107] T. Shi, D. E. Chang, and J. I. Cirac, Multiphoton-scattering theory and generalized master equations, *Phys. Rev. A* **92**, 053834 (2015).
- [108] G. Vidal and R. F. Werner, Computable measure of entanglement, *Phys. Rev. A* **65**, 032314 (2002).